iScience

CellPress
OPEN ACCESS

Article

Glycyrrhetinic acid restricts mitochondrial energy metabolism by targeting SHMT2

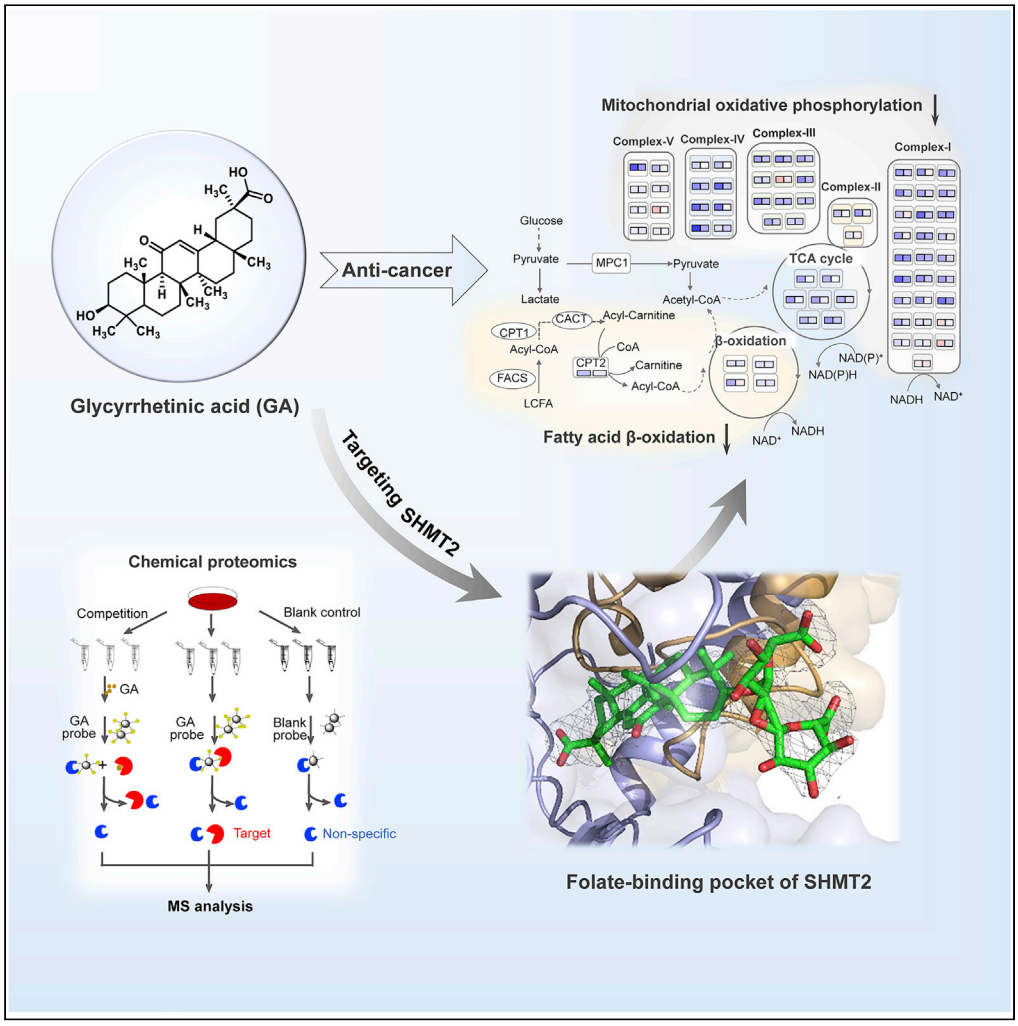

Xiuxiu Jin, Li Li, Qinlu Peng, ..., Yong Peng, Dan Su, Lunzhi Dai

yongpeng@scu.edu.cn (Y.P.)
sudan@scu.edu.cn (D.S.)
lunzhi.dai@scu.edu.cn (L.D.)

Highlights

Mitochondrial protein SHMT2 is a critical target of GA

GA downregulates OXPHOS and FAO through targeting SHMT2

GA targets the folate-binding pocket of SHMT2 and competes with THF

Diamine modification at GA carboxylic group improves anticancer potency

Jin et al., iScience 25, 104349
May 20, 2022
https://doi.org/10.1016/j.isci.2022.104349

iScience

CellPress
OPEN ACCESS

Article

Glycyrrhetinic acid restricts mitochondrial energy metabolism by targeting SHMT2

Xiuxiu Jin,[1,2,7] Li Li,[1,7] Qinlu Peng,[1,7] Chunmei Gan,[1,7] Li Gao,[1] Siyu He,[1] Shuangyan Tan,[1] Wenchen Pu,[1] Yu Liu,[1] Yanqiu Gong,[1] Yuqin Yao,[3] Gang Wang,[4] Xiaohui Liu,[5] Meng Gong,[6] Peng Lei,[1] Huiyuan Zhang,[1] Shiqian Qi,[1] Heng Xu,[1] Hongbo Hu,[1] Biao Dong,[1] Yong Peng,[1,*] Dan Su,[1,*] and Lunzhi Dai[1,8,*]

SUMMARY

Glycyrrhetinic acid (GA) is a natural product of licorice with mitochondria targeting properties and shows broad anticancer activities, but its targets and underlying mechanisms remain elusive. Here, we identified the mitochondrial enzyme serine hydroxymethyltransferase 2 (SHMT2) as a target of GA by using chemical proteomics. Binding to and inhibiting the activity of SHMT2 by GA were validated *in vitro* and *in vivo*. Knockout of SHMT2 or inhibiting SHMT2 with GA restricts mitochondrial energy supplies by downregulating mitochondrial oxidative phosphorylation (OXPHOS) and fatty acid β-oxidation, and consequently suppresses cancer cell proliferation and tumor growth. Crystal structures of GA derivatives indicate that GA occupies SHMT2 folate-binding pocket and regulates SHMT2 activity. Modifications at GA carboxylic group with diamines significantly improved its anticancer potency, demonstrating GA as a decent structural template for SHMT2 inhibitor development.

INTRODUCTION

Mitochondria, the powerhouses of the cell, are indispensable for survival in eukaryotic cells. Dysregulation of mitochondria is a hallmark of cancer and contributes to cancer malignancy (Porporato et al., 2018). Tumors undergo an extensive and highly plastic metabolic reprogramming and mitochondria are the central organelle (Martínez-Reyes and Chandel, 2021). Tumor mitochondria alter their structure and functions to meet the increased energetic and anabolic demands in the hypoxic and acidic microenvironment, such as the increased ability to use oxidative phosphorylation (OXPHOS) and fatty acid oxidation as the source of energy (Porporato et al., 2018). The development of drugs targeting mitochondria-mediated cell proliferation and cell death pathways has become a promising approach for cancer treatment (Fulda et al., 2010; Murphy and Hartley, 2018; Wang et al., 2016; Weinberg and Chandel, 2015).

Natural products are a major source of novel lead compounds for drug discovery and development (Newman and Cragg, 2016). Elucidation of the underlying mechanisms of natural products not only uncovers the cellular functions of their protein targets but also promotes their potential uses in biomedical fields (Cravatt et al., 2008; Grüner et al., 2016; Huber and Superti-Furga, 2016; Neggers et al., 2018; Schenone et al., 2013; Titov et al., 2011). Glycyrrhetinic acid (GA) (Figure 1A), also known as enoxolone, is a biologically active metabolite derived from glycyrrhizin (GZ), a natural small molecule from the most widely used Chinese herb licorice with a long history of pharmaceutical use. It has been well documented that GA and its derivatives have broad biological activities, including anti-inflammatory (Ishida et al., 2013; Kim et al., 2018), antiviral (Wang et al., 2012), antimicrobial (Huang et al., 2016), antiulcer (Aly et al., 2005), hepatoprotective (Jeong et al., 2002; Li et al., 2019), and antitumor activities (Cai et al., 2018). Among them, GA is highly regarded for its remarkable antitumor activity, and exhibits significant cytotoxic activity against diverse cancer cell types *in vitro*, such as cervical cancer cells (Farooqui et al., 2018), colorectal cancer cells (Wang et al., 2017), non-small-cell lung cancer cells (Huang et al., 2014; Song et al., 2014), and hepatocellular carcinoma cells (Satomi et al., 2005). In addition, GA also shows noteworthy activities in multiple cancer cell-derived xenograft (CDX) mouse models (Jinek et al., 2014; Li et al., 2020; Shen et al., 2017; Wang et al., 2015). Although extensive anticancer activities of GA have been described, its underlying molecular mechanisms still remain elusive.

Here, we identified the mitochondrial enzyme serine hydroxymethyltransferase 2 (SHMT2) as a target of GA by chemical proteomics, which was validated *in vitro* and *in vivo*, and further employed the crystal structure

[1]National Clinical Research Center for Geriatrics and Department of General Practice, State Key Laboratory of Biotherapy, West China Hospital, Sichuan University, Chengdu 610041, China

[2]Henan Provincial People's Hospital, Henan Eye Hospital, People's Hospital of Zhengzhou University, Zhengzhou, Henan 450003, China

[3]West China School of Public Health and West China Fourth Hospital, Sichuan University, Chengdu 610041, China

[4]School of Pharmacy, Zunyi Medical University, Zunyi, Guizhou 563003, China

[5]School of Life Sciences, Tsinghua University, Beijing 100084, China

[6]Laboratory of Clinical Proteomics and Metabolomics, Institutes for Systems Genetics, Frontiers Science Center for Disease-related Molecular Network, West China Hospital, Sichuan University, 88 Keyuan South Road, Hi-Tech Zone, Chengdu 610041, China

[7]These authors contributed equally

[8]Lead contact

*Correspondence: yongpeng@scu.edu.cn (Y.P.), sudan@scu.edu.cn (D.S.), lunzhi.dai@scu.edu.cn (L.D.)

https://doi.org/10.1016/j.isci.2022.104349

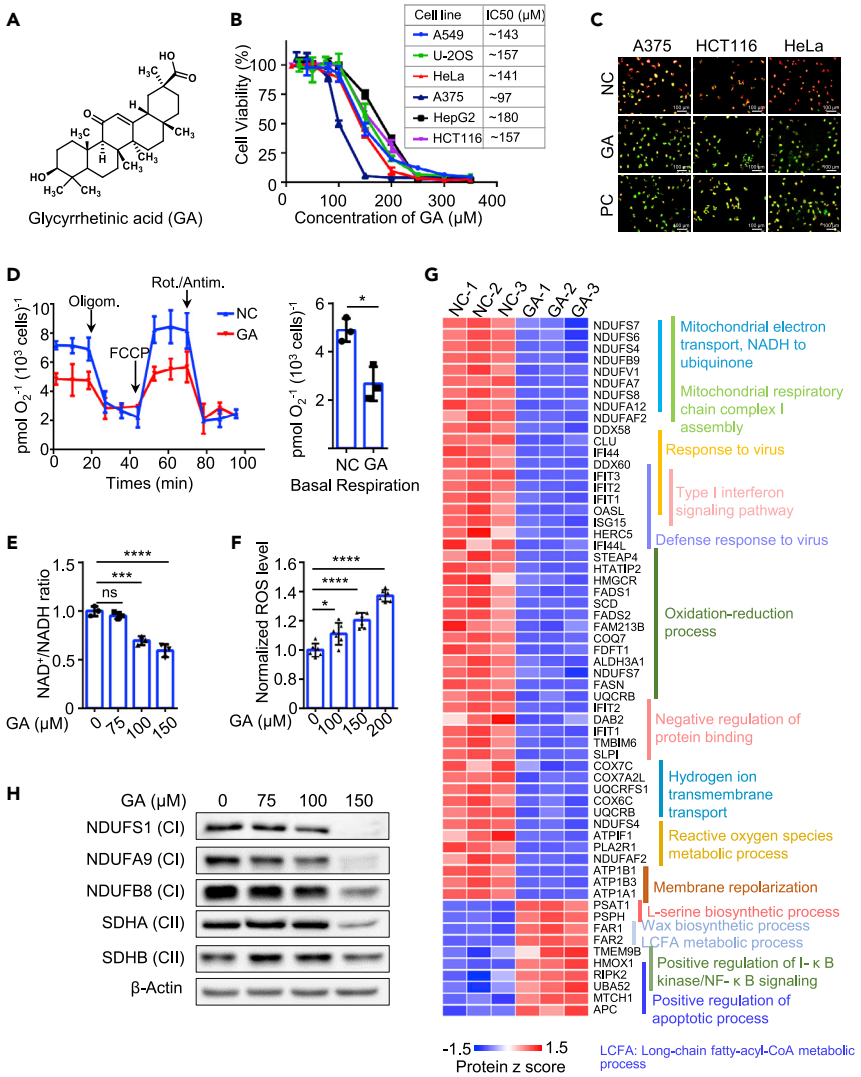

Figure 1. GA causes mitochondrial defects by downregulating mitochondrial functional proteins

(A) The chemical structure of GA.

(B) Growth of multiple cell lines in the presence of increasing concentrations of GA (n = 6). Concentrations of GA used in cell viability analysis were ranging from 10 to 350 μM IC50 values are presented in the mini-table, which was calculated by non-linear least squares curve fitting using Graph Pad Prism version 9.0.0.

(C) Changes in mitochondrial membrane potential of cells. The red-fluorescent aggregates (JC-aggregates) represent high membrane potential and green fluorescence (JC-1 monomers) represents dissipated mitochondrial membrane potential. Cells were exposed to 100 μM GA or control for 12 h before analysis. DMSO was used as negative control (NC) and CCCP was the positive control (PC). The bars in the lower right corners of the pictures indicate 100 μm.

(D) Oxygen consumption rates in HeLa cells exposed with 100 μM GA (or DMSO control) for 12 h before analysis (n = 3). Samples were compared with two-tailed, unpaired Student's *t*-test.

(E and F) NAD^+/NADH ratios (n = 3) (E) and ROS generation (n = 6) (F) in HeLa cells. Cells were exposed to increasing concentrations of GA for 4 h before analysis. Samples were compared with one-way ANOVA analysis with Bonferroni corrected multiple comparisons.

(G) Gene ontology enrichment analysis of the differently expressed proteins induced by 100 μM GA treatment (log_2(fold-change) > 0.321 and $p < 0.05$). Data from biological triplicates are shown. The elements of mitochondrial respiratory chain complex I were most significantly downregulated.

(H) Some downregulated proteins validated by immunoblots. Data are shown as the mean ± SD (error bar). NC, negative control; CCCP, carbonyl cyanide 3-chlorophenylhydrazone; ROS, reactive oxygen species; Oligom., oligomycin; Rot./Antim., Rotenone & antimycin; LCFA, long-chain fatty acid; ns, no significance; CI, respiratory chain complex I; CII, respiration chain complex II; *, $p < 0.05$; **, $p < 0.01$; ***, $p < 0.001$; ****, $p < 0.0001$.

of SHMT2 in complex with GA derivatives to elucidate the mechanism of action of GA. A tight connection between SHMT2 and mitochondrial energy metabolism was built. Moreover, some GA derivatives with improved anticancer activities were synthesized based on the SHMT2 structure. Collectively, this study reveals the detailed mechanism of action of GA, which could be a promising mitochondria-targeting structural lead for targeted therapy of certain cancers, and expands the knowledge of SHMT2 in cancer metabolism.

RESULTS

GA induces mitochondrial defects in cancer cells

To determine the effect of GA on cancer cells, we treated multiple cancer cell lines with GA. Clearly, GA displayed good growth inhibitory effects on cancer cells in a dose-dependent manner (Figure 1B and Table S1), including A549 human lung cancer cell line (IC50, 143 μM), U-2OS human osteosarcoma cell line (IC50, 157 μM), HeLa cervical cancer cell line (IC50, 121 μM), A375 human melanoma cell line (IC50, 97 μM), HepG2 human hepatoma cell line (IC50, 180 μM), and colorectal carcinoma HCT116 (IC50, 171 μM). Given that GA was supposed to exhibit mitochondria-targeting properties (Zhang et al., 2018), we examined the influences of GA on mitochondrial functions. GA treatment caused dramatic decreases in mitochondrial membrane potential (Figure 1C), oxygen consumption rates (Figure 1D and Table S2) and nicotinamide adenine dinucleotide transformation (NAD^+/NADH) (Figure 1E and Table S2), as well as a significant increase in reactive oxygen species (ROS) production in HeLa cells (Figure 1F and Table S2). Collectively, GA can trigger mitochondrial defects in cancer cells and inhibit cell proliferation.

GA significantly downregulates mitochondrial functional proteins

To reveal the signaling pathways responsible for GA-induced mitochondrial stresses in cancer cells, we performed global proteomic profiling in HeLa cells treated with or without 100 μM GA. The extracted total proteins were tryptically digested, followed by isobaric tandem mass tag (TMT) labeling and liquid chromatography with tandem mass spectrometry (LC-MS/MS) analysis (Figure S1A). In total, 6,488 proteins were quantified in biological and technical replicates. Among them, 95 proteins were upregulated and 126 proteins were downregulated after GA treatment (Figure S1B and Table S3). Gene Ontology enrichment analysis of these differentially expressed proteins revealed that mitochondrial respiratory chain complex I assembly was the top downregulated pathway in GA-treated cells (Figures 1G and S1C and Table S3), which was further confirmed by immunoblots (Figure 1H). Moreover, downregulation of these proteins was also observed in other cancer cells, such as A549, A375, HCT116 and HepG2 (Figures S1D–S1G). In addition to the electron transport chain, some other mitochondrial-associated processes, such as the oxidative-reduction process and ROS metabolic process, were also affected by GA treatment. Together, GA impairs mitochondrial functions mainly by downregulating mitochondrial functional proteins.

GA binds to the mitochondrial metabolic enzyme SHMT2

To identify GA targets responsible for the downregulation of mitochondrial functional proteins, we performed chemical proteomics analysis. First, we employed an ultraviolet-crosslinking method to prepare the GA probe (Figure S2A and Table S4), and its successful preparation was verified by Fourier transform infrared spectroscopy (FTIR) and liquid chromatography–mass spectrometry (LC-MS) analysis (Figures S2B–S2C and Table S4). Three parallel pull-down experiments were carried out (Figure 2A). In the first case experiment, the GA probe was incubated with HeLa cell lysate, and the putative GA binding proteins were enriched. In the second competition experiment, the cell lysate was preincubated with excess free GA and then incubated with a GA probe. The proteins that could compete away by free GA were potential targets. In the third blank control, a GA-free probe was used. This control was used to identify non-specific binding proteins. All thepull-down experiments were performed in triplicate, and the pull-down proteins were analyzed by MS. The MS data showed that both SHMT2 and coproporphyrinogen oxidase (CPOX) had the highest abundance and could be efficiently pulled down by the GA probe. Most importantly, the potential SHMT2-GA and CPOX-GA interaction could be completely disrupted by free GA (Figure 2B and Table S5), indicating that these proteins were most likely GA targets. Furthermore, the protein-protein interaction (PPI) analysis of pulled-down proteins showed that many identified proteins known to interact with SHMT2 were also pulled down by GA but with less competition efficiency or fewer interacting proteins (such as CPOX), suggesting that SHMT2 was more likely a GA target than other proteins (Figure 2C). Apart from this evidence, it has been reported that SHMT2-mediated one-carbon metabolism and the electron transport chain are closely coupled (Cuthbertson et al., 2021; Tedeschi et al., 2013),

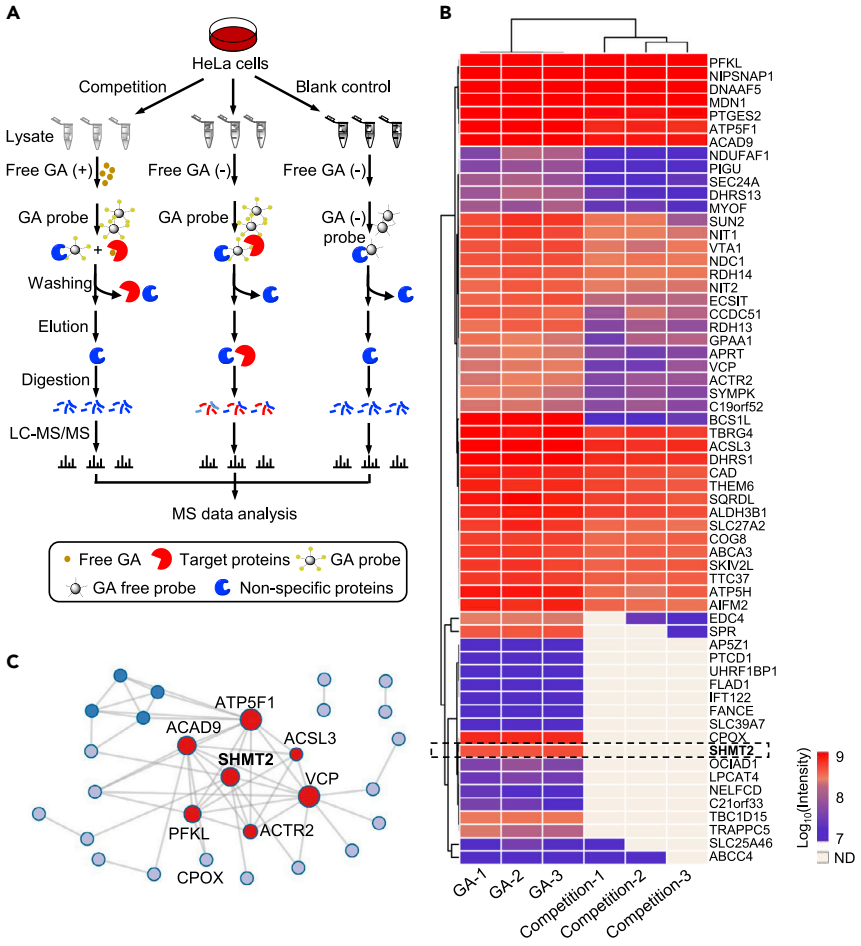

Figure 2. Target identification of GA by chemical proteomics

(A) The workflow of chemical proteomics for target identification of GA. In case experiment (middle), the GA probe was incubated with HeLa cell lysate, and the putative GA binding proteins were enriched. In competition experiment (left), the cell lysate was preincubated with excess free GA and then incubated with a GA probe. The proteins that could compete away by free GA were potential targets. In blank control (right), a GA-free probe was used. This control was used to identify non-specific binding proteins. Each experiment was performed in triplicate, and the pull-down proteins were analyzed by MS.

(B) The heatmap shows the target candidates pulled down by the GA probe. Proteins with p value <0.01 (GA-probe/competition, Student's t-test) and average intensity ratio >1.5 (GA-probe/competition) were chosen as target candidates of GA. Data from biological triplicates are shown.

(C) The protein-protein interaction (PPI) analysis of the target candidates by Metascape. SHMT2 has the most interacting proteins with lower protein intensity and fewer unique peptides compared with SHMT2. ND, not detected.

consistent with the observed mitochondrial phenotypes. Therefore, we assume that the mitochondrial one-carbon metabolism enzyme SHMT2 is a potential target candidate for GA.

Validation of SHMT2 as a target of GA *in vitro*

To verify the interaction between GA and SHMT2, we performed a retro-pull-down experiment using purified SHMT2 as bait and found that GA was indeed effectively enriched by SHMT2 (Figure 3A and Table S6). Next, we characterized their binding affinities by surface plasmon resonance (SPR) assay. As indicated by Figure 3B, the binding affinity between GA and SHMT2 was 2.90 μM. Moreover, the cellular thermal shift (CETSA) assay presented the thermal stability of SHMT2 under treatment with GA (100 μM), and the fluorescence-quenching assay indicated the binding interaction of GA and SHMT2 (Figures 3C and 3D). SHMT2 is an enzyme that catalyzes serine/glycine conversion in folate-mediated one-carbon metabolism. To explore whether GA could inhibit the catalytic activity of SHMT2 *in vitro*, we examined the enzyme

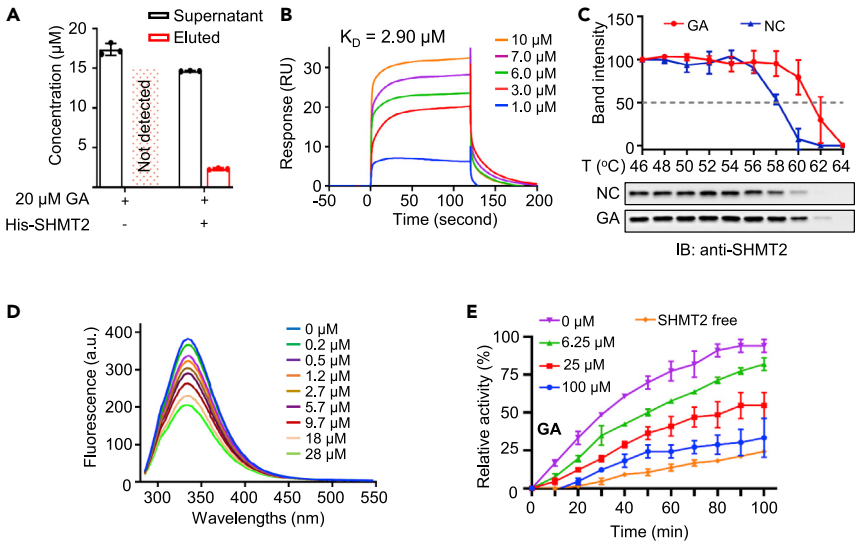

Figure 3. Systematic validation of SHMT2 as a target of GA *in vitro*

(A) Retro-pull-down experiments (n = 3). GA can be pulled down by the purified His-SHMT2-conjugated beads but not blank beads.

(B) The SPR assays show the *in vitro* interaction between GA and SHMT2. The dissociation constant value (K_D) is 2.90 μM.

(C) The CETSA experiments show that SHMT2 becomes more stable as the temperature increases in the sample treated with GA (n = 3).

(D) The fluorescence-quenching experiments show that the fluorescence is gradually quenched as the concentration of GA increases.

(E) Assessment of the *in vitro* enzymatic activity of SHMT2 affected by GA (n = 3). As the concentration of GA increases, the enzymatic activity of SHMT2 is gradually inhibited and almost completely inhibited at 100 μM GA. T, temperature; SPR, surface plasmon resonance; CETSA, cellular thermal shift. Data are shown as the mean ± SD (error bar).

activities of SHMT2 with gradient concentrations of GA as reported (Wei et al., 2018). The results showed that the activity of SHMT2 indeed decreased with increasing concentrations of GA, indicating that GA was an inhibitor that suppressed SHMT2 activity *in vitro* (Figure 3B and Table S6). Taken together, SHMT2 is a target of GA *in vitro*.

Evaluation of SHMT2 as a target of GA in cells

To prove that SHMT2 is a target of GA in cells, we compared the GA sensitivity of cells with wild-type (WT) or without SHMT2 expression (KO), and found that the SHMT2 KO HeLa cells became less sensitive to GA treatment (Figures 4A and S3A and Table S8). The changes in NAD^+/NADH ratios (Figure 4B and Table S2) and ROS production (Figure 4C and Table S2) in SHMT2 KO HeLa cells after GA treatment were measured, and we found that the changes were not as obvious as those in SHMT2 WT HeLa cells. Moreover, the oxygen consumption rates were inhibited in response to GA treatment and SHMT2 depletion (Figure 4D and Table S2). Similar results were also observed in the SHMT2 knockdown A375 melanoma cell line (Figures S3B–S3C). The above assays indicate that SHMT2 is a target of GA in cells. To examine whether overexpression of SHMT2 could rescue the levels of mitochondrial respiratory complex I proteins and thus recover the functions of the electron transport chain, SHMT2 was transfected into GA-treated HeLa cells. As expected, the proteins levels could be partially recovered (Figure 4E).

Exogenous formate was reported to rescue one-carbon metabolism and cell growth defects caused by SHMT2 depletion by providing one-carbon units directly to the THF cycle (Minton et al., 2018; Tibbetts and Appling, 2010). We asked whether formate addition would be able to rescue the cell phenotype presented by SHMT2 inhibition with GA. Our results showed that formate supplementation could rescue GA- or SHMT2 KO-induced cell arrest ($p < 0.05$, Figure 4F), consistent with our conclusion that SHMT2 is a target of GA. The intracellular ATP level is mainly affected by mitochondrial oxidative phosphorylation (OXPHOS) (Xu et al., 2005). Serine/glycine conversion also supports the methionine cycle through *de novo* ATP synthesis, and abnormal serine metabolism can dramatically reduce ATP levels (Maddocks et al., 2016). We found that formate treatment could also partially rescue the ATP levels in GA-treated or SHMT2 KO cell

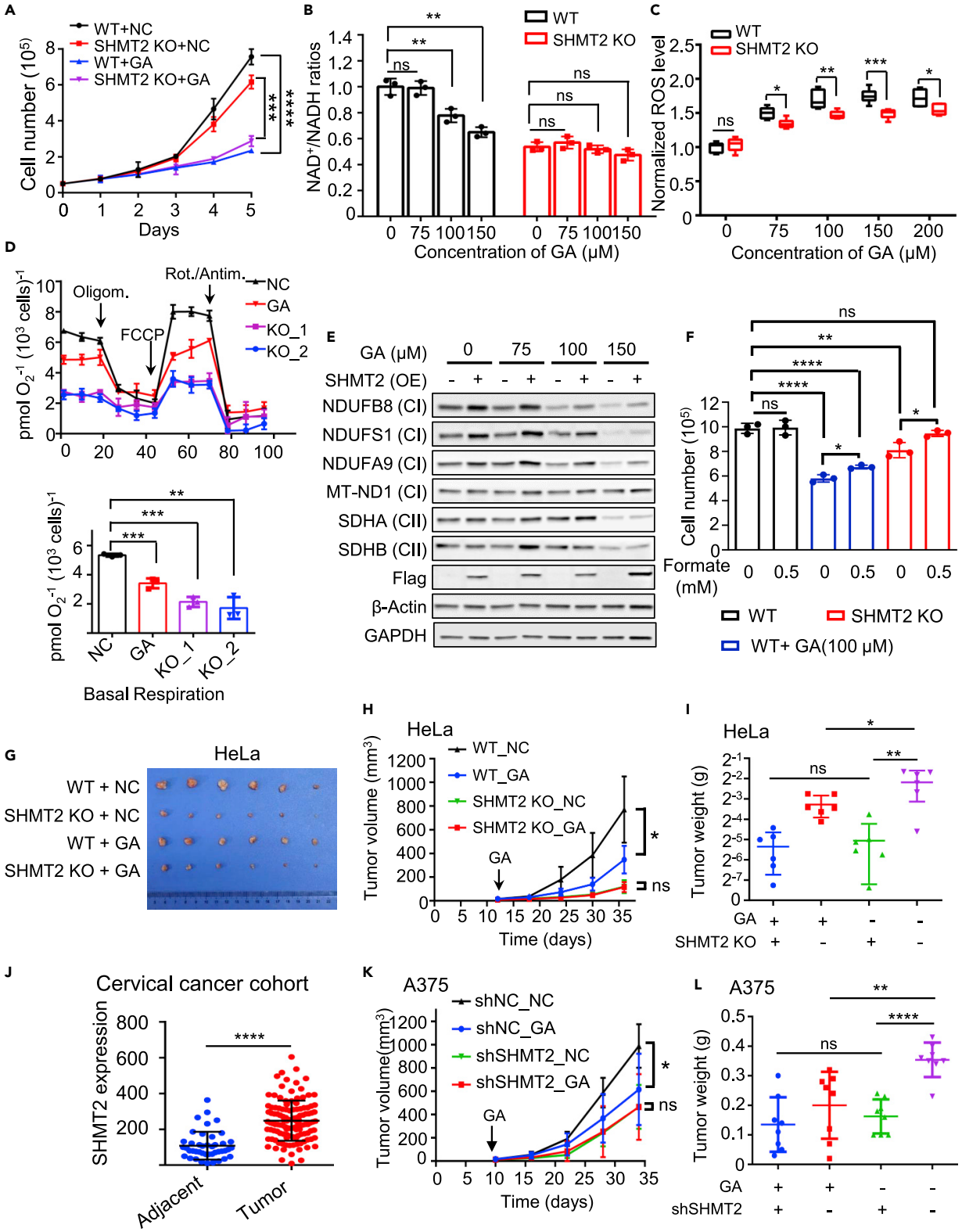

Figure 4. Evaluation of SHMT2 as a target of GA in cell and mouse models

(A) HeLa cell proliferation was affected by GA treatment in SHMT2 KO and WT cells (n = 3). Cells were exposed to 100 μM GA (or DMSO control) and counted every day over a 5-day period. GA shows higher inhibitory potency in SHTM2 WT HeLa cells than in SHTM2 KO HeLa cells.

Figure 4. *Continued*

(B) The NAD^+/NADH ratios affected by GA treatment in SHMT2 KO and WT cells (n = 3). Cells were exposed to increasing concentrations of GA for 4 h before analysis. In SHMT2 WT but not SHMT2 KO HeLa cells, GA reduces the ratios of NAD^+/NADH.

(C) The ROS levels affected by GA treatment in SHMT2 KO and WT cells (n = 6). Cells were exposed to increasing concentrations of GA for 4 h before analysis. ROS production is less sensitive to GA treatment in SHMT2 KO HeLa cells than in SHMT2 WT HeLa cells.

(D) The oxygen consumption affected by GA treatment or SHMT2 KO (n = 3). Cells were exposed to 100 μM GA (or DMSO control) for 12 h before analysis. Similar changing patterns were observed in HeLa cells in response to GA treatment and SHMT2 depletion.

(E) Immunoblotting analysis of mitochondrial proteins. The downregulation of some mitochondrial proteins induced by GA treatment can be partially rescued by overexpression of SHMT2.

(F) Proliferation of SHMT2 KO or WT HeLa cells treated with 0.5 mM formate, 100 μM of GA or its DMSO control for 3 days (n = 3).*p*values were determined by two-way ANOVA analysis with Bonferroni corrected multiple comparisons.

(G) Tumors from CDX mouse models 35 days after injection with HeLa (WT or SHMT2-KO) cells (n = 6).

(H and I) The tumor volume (H) and weight (I) affected by 30 mg/kg GA treatment in mice injected with SHMT2 KO and WT HeLa cells. GA (30 mg/kg) showed almost no inhibitory effects on mice injected with SHMT2 KO HeLa cells. The arrow points to the beginning of GA administration.

(J) The expression of SHTM2 in cervical cancer. The expression of SHMT2 in tumors was significantly higher (adjacent tissues, n = 42; tumors, n = 119). Samples were compared with two-tailed, paired Student's *t*-test.

(K and L) The tumor volume (K) and weight (L) affected by 30 mg/kg GA treatment in mice injected with shSHMT2 and shNC A375 cells (n = 8). GA showed almost no inhibitory effects on mice injected with shSHMT2 A375 cells. The arrow points to the beginning of GA administration. Oligom., oligomycin; Rot./Antim., Rotenone & antimycin; ns, no significance; CDX, cancer cell-derived xenograft; The data are shown as the mean ± SD (error bar). p values were determined by one-way ANOVA analysis with Bonferroni corrected multiple comparisons with no special instructions; $p < 0.05$; **, $p < 0.01$; ***, $p < 0.001$; ****, $p < 0.0001$.

cultures, consistent with our observations that GA could downregulate OXPHOS and affect one-carbon metabolism by targeting SHTM2 ($p< 0.05$, Figure S3D).

Evaluation of SHMT2 as a target of GA in xenograft mice

Next, we evaluated SHMT2 as a target of GA in CDX mouse models. To obtain unbiased results, SHMT2 WT and KO HeLa cells were injected subcutaneously into both sides of each mouse (Figure S3E). After 12 days, GA was administered intraperitoneally once every 3 days at a dose of 30 mg/kg. We found that GA administration dramatically suppressed the tumor growth of SHMT2 WT cells, but had little effect on the tumor growth of SHMT2 KO cells (Figures 4G–4I and Table S8). Immunohistochemical staining of a cervical cancer tissue microarray showed that tumorous tissues had much higher SHMT2 expression than nontumorous tissues (paired Student's *t*-test, $p< 0.001$) (Figure 4J and Table S9), indicating that SHMT2 might be a potential target for cervical cancer treatment. Similar results were also observed in CDX mouse models injected with A375 (Figures 4K–4L, S3F–S3G, and Table S8) and HCT116 cells (Figures S3H–S3J and Table S8). Taken together, GA inhibited tumor growth in xenograft mice, and the inhibitory effects were compromised in mice injected with SHMT2 KO cells, again demonstrating that SHMT2 is a GA target.

GA restricts mitochondrial energy supplies by downregulating OXPHOS and FAO

If SHMT2 is a critical target of GA, the cellular proteomic change patterns induced by GA inhibition or SHMT2 inhibition should be very similar. Therefore, we compared proteomic data between SHMT2 KO and GA-treated HeLa cells. Strikingly, a good significant association was observed in the altered proteins, and the Pearson correlation coefficient ranged between 0.61 and 0.66, indicating that the proteomic changes induced by GA were largely because of its inhibition of SHMT2 (Figure 5A and Table S7).

To investigate the influence of targeting SHMT2 by GA treatment, the proteomic data were analyzed with DAVID 6.8 and gene set enrichment analysis (GSEA, with tumor hallmark database). KEGG pathway and tumor hallmark analysis revealed that OXPHOS was downregulated significantly both in GA-treated and SHMT2 KO cells (Figures 5B and S4A). Furthermore, the shared downregulated biological processes were mainly mitochondrial respiratory chain complex assembly, mitochondrial electron transport chain, redox and reactive oxygen metabolism (Figures 5C and S4B). Correspondingly, mitochondrial respiratory electron transport chain-associated proteins were found to be synchronously downregulated in both GA-treated and SHMT2 KO cells, consistent with the phenotypic results (Figure 5D). In addition, proteins belonging to the TCA cycle showed decreased patterns, yet increased cellular lactate levels were observed upon SHMT2 suppression (Figure S4C). In addition, SHMT2 is essential for maintaining redox balance and cell survival, and SHMT2 repression impairs antioxidant production and results in a significant increase in ROS under hypoxia, usually leading to cell death (Balsa et al., 2020; Yang et al., 2020; Ye et al., 2014). In our study, we also found that the production of ROS induced by GA might be associated with SHMT2 (Figures 4C and S3C). Therefore, we examined whether GA-induced ROS would cause cell apoptosis

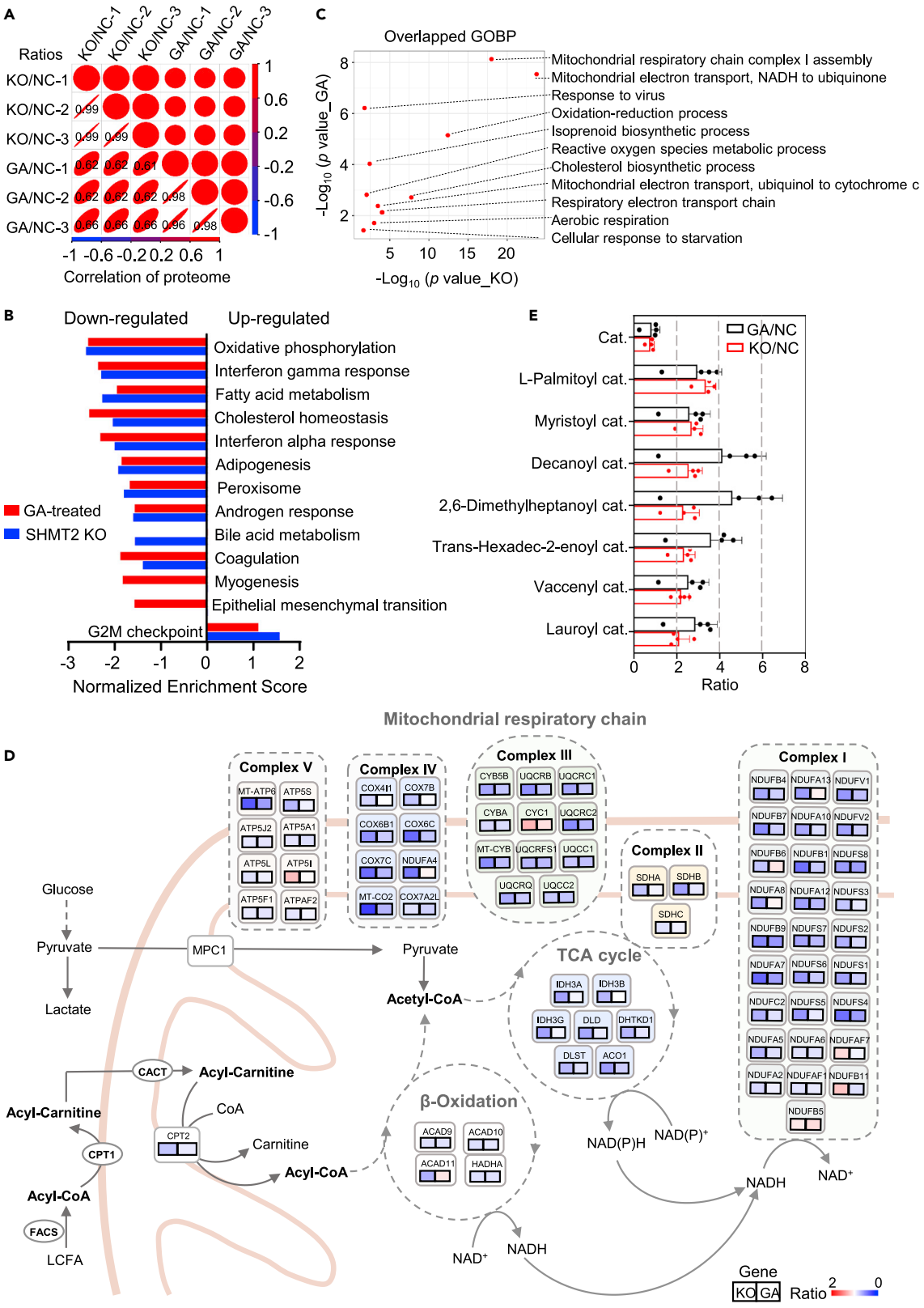
A
Ratios
KO/NC-1
KO/NC-2
KO/NC-3
GA/NC-1
GA/NC-2
GA/NC-3
0.99
0.99 0.99
0.62 0.62 0.61
0.62 0.62 0.62 0.98
0.66 0.66 0.66 0.96 0.98
1
0.6
0.2
-0.2
-0.6
-1
-1 -0.6 -0.2 0.2 0.6 1
Correlation of proteome
C
Overlapped GOBP
-Log10 (p value_GA)
-Log10 (p value_KO)
Mitochondrial respiratory chain complex I assembly
Mitochondrial electron transport, NADH to ubiquinone
Response to virus
Oxidation-reduction process
Isoprenoid biosynthetic process
Reactive oxygen species metabolic process
Cholesterol biosynthetic process
Mitochondrial electron transport, ubiquinol to cytochrome c
Respiratory electron transport chain
Aerobic respiration
Cellular response to starvation
B
Down-regulated
Up-regulated
GA-treated
SHMT2 KO
Oxidative phosphorylation
Interferon gamma response
Fatty acid metabolism
Cholesterol homeostasis
Interferon alpha response
Adipogenesis
Peroxisome
Androgen response
Bile acid metabolism
Coagulation
Myogenesis
Epithelial mesenchymal transition
G2M checkpoint
Normalized Enrichment Score
E
GA/NC
KO/NC
Cat.
L-Palmitoyl cat.
Myristoyl cat.
Decanoyl cat.
2,6-Dimethylheptanoyl cat.
Trans-Hexadec-2-enoyl cat.
Vaccenyl cat.
Lauroyl cat.
Ratio
D
Mitochondrial respiratory chain
Complex V
Complex IV
Complex III
Complex II
Complex I
Glucose
Pyruvate
Lactate
MPC1
Acetyl-CoA
TCA cycle
β-Oxidation
CACT
Acyl-Carnitine
CPT1
CPT2
CoA
Carnitine
FACS
LCFA
NAD(P)H
NAD(P)+
NADH
NAD+
Gene
KO GA
Ratio

Figure 5. Global investigation of signaling pathways affected by GA treatment in cancer cells

(A) Proteome-wide analysis of changing patterns in response to 100 μM GA treatment for 48 h and SHMT2 KO. The correlations between the different groups were calculated using corrplot R code (Pearson correlation analysis). A very good correlation is observed.

(B) The signaling pathways affected by GA treatment or SHMT2 KO. Most enriched pathways showed similar changing patterns in response to GA treatment or SHMT2 KO.

(C) The overlapping analysis of GOBP enrichment results upon GA treatment and SHMT2 KO.

(D) Changes in the OXPHOS, TCA cycle and FAO pathways in response to GA treatment or SHMT2 KO. Most proteins in these pathways were downregulated. Thefold change is calculated by KO/NC (left) or GA/NC (right). MPC represents the mitochondrial pyruvate carrier.

(E) The abundance of acylcarnitines and carnitine in response to SHMT2 repression. The transport of acylcarnitines into the mitochondrial inner membrane is affected, leading to the accumulation of cellular acylcarnitines (n = 4). Cat. is short for carnitine. Data are shown as the mean ± SD (error bar).

and reduce cell growth. Flow cytometric assays for apoptosis in response to GA treatment and SHMT2 KO showed that neither GA treatment nor SHMT2 KO could induce apoptosis in our cultured conditions, indicating that observed slower cell proliferation was not because of increased cell apoptosis (Figures S4D–S4G). Collectively, GA targeting SHMT2 restricts energy metabolism by downregulating mitochondrial OXPHOS and redox metabolism.

Fatty acid β-oxidation (FAO) is also an important energy source for maintaining cell survival. It was found that some proteins involved in FAO were also downregulated (Figure S4H). To the best of our knowledge, the relationship between SHMT2 and FAO is still largely unknown. To achieve this goal, we performed untargeted metabolomics to shed light on the underlying mechanism. Many acylcarnitines were detected in both SHMT2 KO and GA-treated cells (Figure 5E and Table S10). The effective transport of long-chain fatty acids into mitochondria is a critical step for FAO and the maintenance of cellular energy homeostasis (Eaton, 2002). Because cellular accumulation of acylcarnitines was observed upon GA treatment or SHMT2 depletion, we assumed that the transformation of acylcarnitines to acyl-Co-As might become an issue. Our proteomics data showed that CPT2, a key regulator of acylcarnitine conversion to acyl-CoA (Schoonemman et al., 2013), was significantly downregulated when SHMT2 was depleted or inhibited (Figures 5D and S4H and Table S7). Meanwhile, the upstream CPT1A was upregulated, suggesting SHMT2 controlled FAO by regulating the transformation of acylcarnitines to acyl-Co-As. Moreover, proteins involved in the whole FAO process, including *de novo* synthesis of fatty acids, long-chain fatty acid transportation, and β-oxidation, were dramatically downregulated (Figure S4H). This finding indicated that GA may block the FAO process by targeting SHMT2. Taken together, GA binds to SHMT2 and may restrict energy metabolism by downregulating mitochondrial OXPHOS and FAO, thus suppressing cell proliferation.

Combined analysis of the transcriptome and proteome data

Next, we asked whether the effects are transcriptionally or translationally regulated. To achieve this goal, we performed RNA sequencing on GA-treated and SHMT2 KO HeLa cells (Table S7). The results showed that there was no correlation in changing patterns between GA-treated and SHMT2-KO cells at the transcriptional level (Figures S5A and S5B), which was consistent with previous findings that inhibiting SHMT2 could affect mitochondrial protein expression at the translational level (Morscher et al., 2018). Specifically, OXPHOS-related genes showed a positive correlation trend at the protein level (Pearson correlation coefficient R = 0.6445), yet the changes in these genes at the transcriptional level were still randomly dispersed without correlation (Pearson correlation coefficient R = −0.0479) (Figure S5C). These results indicated that GA-treated and SHMT2 KO cells shared a similar changing pattern in the proteome, but not in the transcriptome. As a comparison, we found that the Pearson correlation coefficients of proteomic data between CPOX KO and GA-treated HeLa cells ranged from 0.24 to 0.49 (Figure S5D), much lower than those between SHMT2 KO and GA-treated HeLa cells (0.61–0.66) (Figure 5A). Moreover, the OXPHOS pathway was almost unchanged in response to CPOX KO (Figure S5E), indicating that CPOX might be a less important target of GA than SHMT2. Taken together, GA-targeted SHMT2 mainly resulted in mitochondrial respiratory deficiency and inhibition of OXPHOS in HeLa cells, and the effects were not at the transcriptional level.

Structural insights into the mechanism of action of GA

Restricted by the solubility of GA, we failed to obtain the crystal structure of SHMT2-GA. However, we solved the structure of a GA water-soluble derivative (GZ) in complex with the SHMT2 dimer in one asymmetric unit (Table S11). The quaternary structure of the SHMT2-GZ complex was calculated by using EPPIC (Evolutionary Protein-Protein Interface Classifier) to estimate the biological relevance of SHMT2 assembly, in which two SHMT2 dimers form a stable symmetric tetramer (Table S12). Each SHMT2 dimer binds two GZ

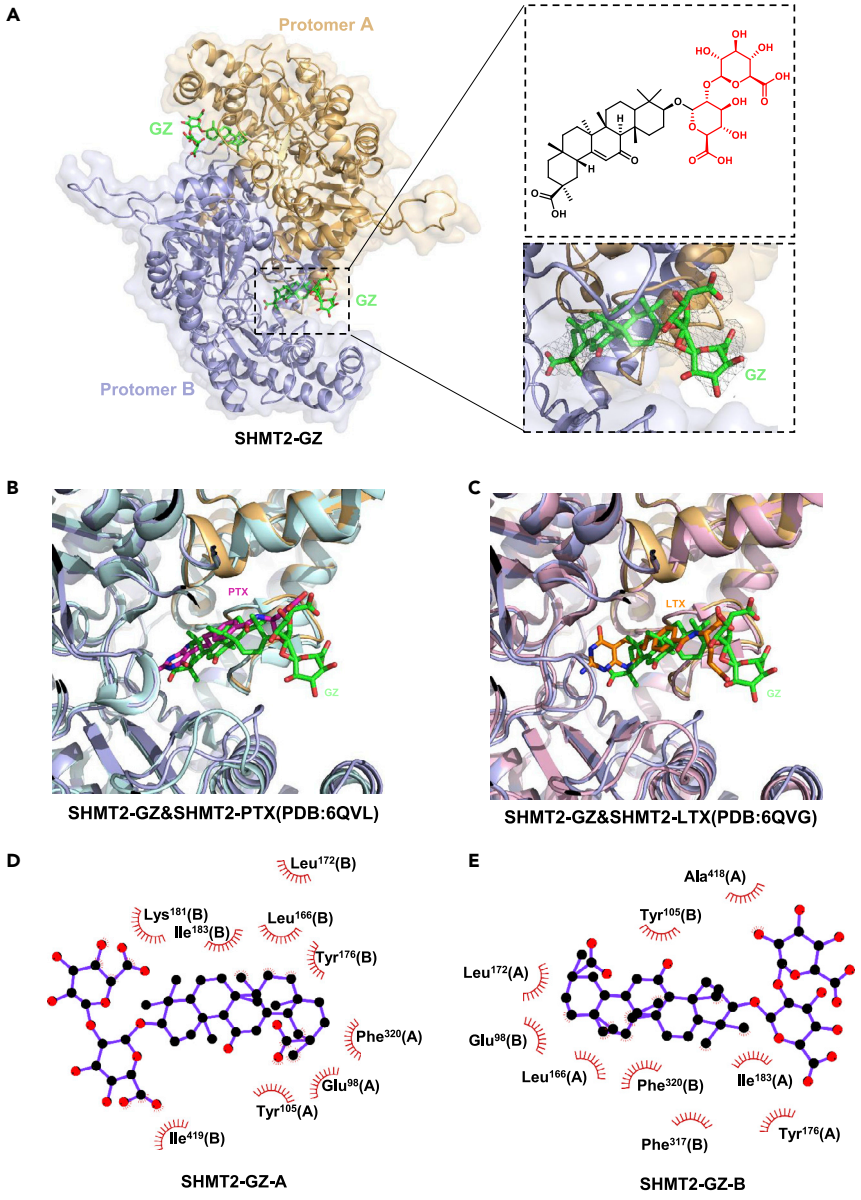

Figure 6. The structure of SHMT2 in complex with GZ

(A). Detailed crystal structure information of SHMT2-GZ. The details of GZ are shown on the right. The 2Fo-Fc electron density map of GZ is contoured at the 1.0σ level and shown in gray80.

(B) Superposition of hSHMT2-GZ and hSHMT2-PTX.

(C) Superposition of hSHMT2-GZ and hSHMT2-LTX. The ligands GZ, LTX, PTX are shown as sticks, colored green, orange, and magenta. LTX, Lometrexol; PTX, pemetrexed. The PDB ID codes of hSHMT2-LTX (colored pink) and hSHMT2-PTX (colored pale cyan) are 6QVG and 6QVL, respectively.

(D and E) The 2D contact map of SHMT2 and GZ built in ligplot+. Ligand atoms that participate in hydrophobic interactions surrounded by red "hedgehogs" (each such atom can form several hydrophobic contacts with different protein atoms). Protein residues involved only in hydrophobic interactions with the ligand (not forming hydrogen bonds with it) are shown as a large red "hedgehog".

molecules, which located in the crevice between two monomers. The electron density of GZ was identified in both binding pockets of the SHMT2 dimer (Figure 6A). The structural superposition between the structure of SHMT2-GZ complex and previously solved SHMT2-antifolate structures (PDB ID code: 5V7I, 6QVG, and 6QVL) revealed that the triterpenoid aglycone of GZ with similar structure of GA, and classic antifolates such as lometrexol (LTX), pemetrexed (PTX) for cancer treatment both bind SHMT2 in close to the folate

binding site (Figures 6B and 6C). However, the disaccharide of GZ is stuck outside of the entrance and may prevent GZ from reaching the bottom of the pocket compared with the other two inhibitors (Scaletti et al., 2019). Each GZ-binding site of SHMT2 was located in a dimeric interface comprised of key residues Leu^{166}, Leu^{172}, Tyr^{176}, and Ile^{183} from one protomer and residues Glu^{98}, Tyr^{105}, Phe^{317}, and Phe^{320} from another protomer (Figures 6D and 6E). Comparison of the SHMT2-GZ structure with apo SHMT2 (PDB ID: 4PVF) indicates that a loop region from residues Asn^{410}-Gly^{423} flipped over and then partly closed the entrance of the folate-binding site when GZ entered the pocket of SHMT2 (Figures S6A and S6B). Furthermore, we identified that GA had a very similar binding affinity as THF (GA: K_D = 2.90 μM; THF: K_D = 3.51 μM) (Figure S6C) and inhibited the enzyme activity of SHMT2. Thus, we speculated that GA might compete with THF as an antifolate inhibitor similar to LTX and PTX.

Chemical derivatization of GA at the carboxylic group improves the inhibitory potency

The crystal structure indicated that the carboxylic group (R_1) of the core structure of GA inserted into the cave of the SHMT2 pocket, and the modified hydroxyl group (R_2, e.g., two molecules of glucuronic acids) extended outside of the pocket. To explore the relationships between R_1 or R_2 and the anticancer potency of GA, R_1-modified GA derivatives were synthesized and then compared with GA or its derivatives modified in R_2. As shown in Figure 7A, diamine-modified GA derivatives including GEN, GPN, and GBN, were obtained by amidation at R_1 by ethylenediamine, propylenediamine, and butylenediamine separately (Schwarz et al., 2014) (Figures S7A–S7I). Carbenoxolone (CBX) and GZ are GA derivatives modified by succinic acid and two molecules of glucuronic acids in R_2, respectively. As indicated by initial cellular experiments, the IC50 values of GA in most cancer cell lines were approximately 100 μM. It was found that amine derivatives in R_1, especially GPN, exhibited much better inhibitory potency in both HeLa and A357 cells (Figures 7B and 7C and Table S1), whereas GZ and CBX showed little effect on the proliferation of these cell lines. Consistent with the cellular results, the binding affinity between GZ (or CBX) and SHMT2 decreased, whereas GPN showed slightly improved binding affinity with SHMT2 [GPN (K_D = 2.14 μM) < GA (K_D = 2.90 μM) < CBX (K_D = 15.1 μM) < GZ (K_D = 43.3 μM)]. Further studies showed that some proteins of the mitochondrial respiration complex were downregulated in HeLa cells treated with 40 μM GEN, GPN, or GBN (Figure 7H). Cellular ATP production could also be dramatically suppressed with less diamine-modified GA derivatives. Therefore, these derivatives might be more potent inhibitors to restrict energy metabolism (Figure 7I and Table S2). Collectively, these findings suggest that chemical modifications at the carboxylic group of GA with diamines could significantly improve the anticancer potency of GA, indicating that GA may be a good template for further SHMT2 inhibitor design.

DISCUSSION

GA is a natural product possessing broad antitumor activities and mitochondrial-targeting properties (Cai et al., 2018; Huang et al., 2014; Li et al., 2020; Zhang et al., 2018), yet its targets and underlying mechanisms remain to be explored. In this study, we revealed SHMT2 as a critical target of GA and clarified the underlying mechanism of action. A number of novel findings and breakthroughs were achieved. First, we identified the mitochondrial protein SHMT2 as a critical target of GA, which was validated by a series of experiments both *in vitro* and *in vivo*. Second, according to the multiomics results, we revealed that GA bound to SHMT2 and inhibited mitochondrial energy metabolism by downregulating OXPHOS and FAO and might consequently suppress cell proliferation and tumor growth. Moreover, we found that the inhibitory effects of GA on OXPHOS might be regulated at the translational level. Third, the crystal structure of SHMT2 with GZ indicated that GA might inhibit the activity of SHMT2 by targeting the folate-binding pocket of SHMT2 and competing with THF. Finally, we disclosed that chemical modifications at the carboxylic group of GA with diamines could significantly improve the anticancer potency of GA, indicating that GA was a good structural template for the development of SHMT2 inhibitors.

The SHMT2 enzyme is usually highly expressed in cancers, and SHMT2 deficiency leads to mitochondrial respiration defects (Lucas et al., 2018; Minton et al., 2018; Morscher et al., 2018; Tani et al., 2018, 2019), which makes SHMT2 a promising target for cancer treatment (Ding et al., 2013; Kim et al., 2015; Liu et al., 2021; Nguyen et al., 2021; Wei et al., 2018; Yang et al., 2018). The mitochondrial respiration system is a well-known machine that generates ATP in mammalian cells. Our results showed that GA significantly downregulated OXPHOS, and the regulation of OXPHOS protein expression was at the transactional level but not the transcriptional level. Although downregulation of OXPHOS is universal in most cancers(Xu et al., 2020), more evidence shows that the survival of cancer cells in certain cancer subtypes, such as breast cancer deficient in RB1 (RB transcriptional corepressor 1) (Jones et al., 2016), the OXPHOS-high subset of

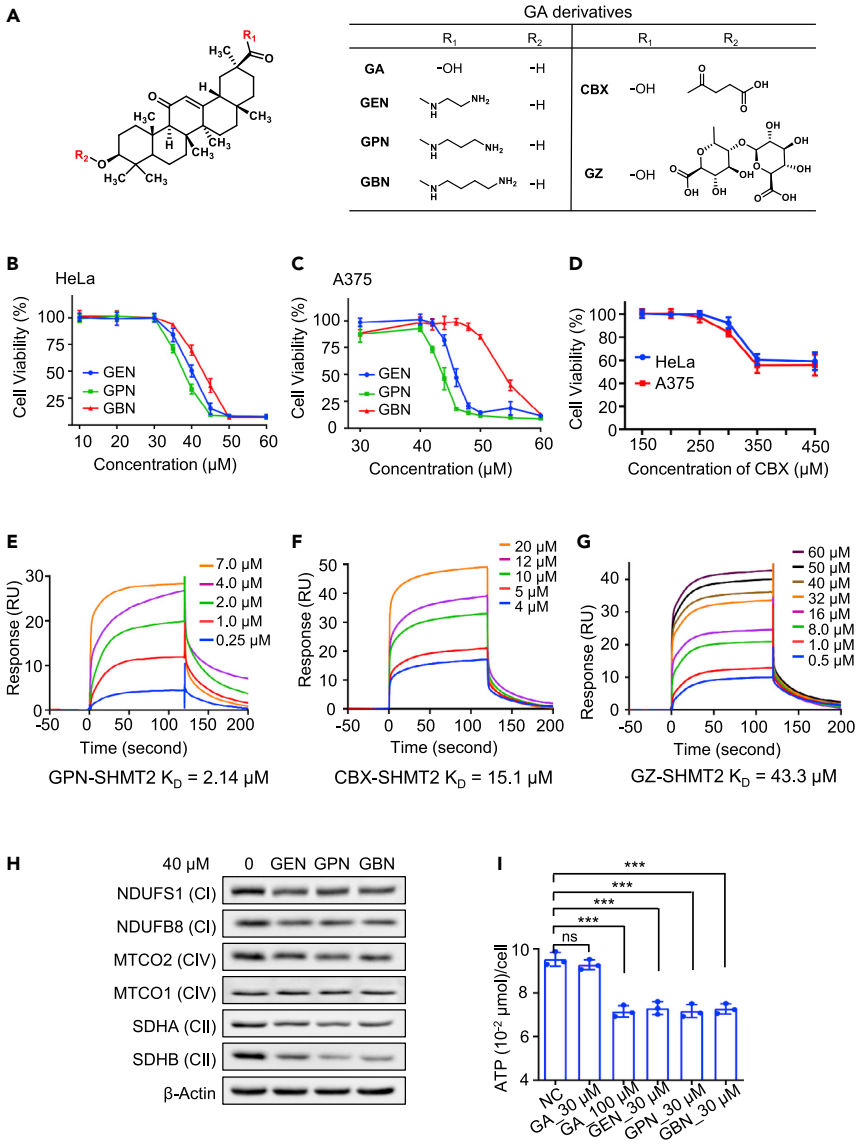

Figure 7. Chemical derivatization of GA at the carboxylic group improves the inhibitory potency

(A) The chemical structures of GA derivatives. R in red represents an unspecified molecule part. GA derivatives modified in R_1 or R_2 are listed in the table on the right.

(B and C) The inhibiting concentrations of the GA derivatives GEN, GPN and GBN in A375 (B) and HeLa (C) cells (n = 6). The IC_{50} values of GEN, GPN and GBN dramatically decreased compared with that of GA.

(D) The inhibiting concentration of CBX in A375 and HeLa cells.

(E–G) SPR assays show the interactions of GPN-SHMT2 (E), CBX-SHMT2 (F) and GZ-SHMT2 (G). The K_D value between GPN and SHMT2 was 2.14 μM, between CBX and SHMT2 was 15.1 μM, and between GZ and SHMT2 was 43.3 μM.

(H) Immunoblots of mitochondrial proteins associated with OXPHOS in response to GEN, GPN and GBN in HeLa cells. The expression of these proteins was slightly downregulated after 40 μM drug treatment.

(I) ATP production affected by GA and its derivatives. The GA derivatives GEN, GPN and GBN show much higher inhibitory potency on cellular ATP production (n = 3). CBX, carbenoxolone; p values were determined by one-way ANOVA analysis with Bonferroni corrected multiple comparisons, and the data are shown as the mean ± SD (error bar); ns, no significance; $p < 0.05$; **, $p < 0.01$; ***, $p < 0.001$; ****, $p < 0.0001$.

diffuse large B-cell lymphomas (DLBCL) (Caro et al., 2012), KRas (GTPase KRas) ablated-pancreatic ductal adenocarcinoma (PDAC) (Viale et al., 2014), non-small-cell lung cancer (NSCLC) with LKB1 (liver kinase B1) deficiency (Shackelford et al., 2013), and melanoma with BRAF (serine/threonine-protein kinase B-raf) mutation (Haq et al., 2013), is dependent on the OXPHOS pathway. In addition, some malignant hypoxic solid

tumors are expected to be sensitive to OXPHOS restriction because the reduced oxygen consumption rate will increase the retention of oxygen throughout the tumor and subsequently decreasing tumor hypoxia (Ashton et al., 2018). Therefore, selective inhibition of OXPHOS in the above cancer subtypes may be effective in suppressing tumor malignance. In addition, FAO is another critical metabolic pathway that provides cells energy to maintain cell survival. It not only generates acetyl-CoA that further enters the TCA cycle, but also produces NADH and $FADH_2$ for energy production in the OXPHOS pathway (Houten et al., 2016). In fasting proliferating cancer cells, fatty acids are essentially required to sustain membrane biosynthesis (Currie et al., 2013; Li and Zhang, 2016) and serve as a vital energy source in metabolic stress conditions (Butler et al., 2020). Here, we first built a connection between FAO and SHMT2. Inhibiting SHMT2 activity by GA or depleting SHMT2 not only affected the function of the mitochondrial electron transport chain but also reduced FAO by suppressing the transport of fatty acids into the mitochondrial inner membrane (Figures 5D and 5E). The expression of many mitochondrial proteins responsible for FAO is closely dependent on SHMT2 (Figure S6H). Most importantly, loss of SHMT2 functions downregulate CPT2 and resulted in the accumulation of acylcarnitines (Figure 5E). As indicated by Figure 1B, inhibitory activities of GA vary in different tumor cell lines. Specifically, IC50 value of GA on HepG2 cells is comparable to that of non-tumor cells (Figure S8A), indicating that GA may not be suitable for all tumor cells. Considering that GA significantly disrupts energy homeostasis in cancers by inhibiting both OXPHOS and FAO, we assume that GA may act as a therapeutic agent in OXPHOS or FAO dependent cancer subtypes.

In this work, multiple lines of evidence indicated the physical interaction between GA and SHMT2. To understand the structural basis of SHMT2-GA and derivative interactions, we solved the X-ray crystal structure of SHMT2 in complex with GZ. The SHMT2-GZ structure demonstrated that the dimer-of-dimers tetrameric assembly of SHMT2 affords four active binding pockets to GA and its derivatives. Superposition of the binding pockets of SHMT2-antifolate structures with SHMT2-GZ indicates that the overall shape and size of the folate-binding pocket of SHMT2 would be able to accommodate a number of ligands, including folate, LTX, PTX, GA, and derivatives. A previous publication reported that the folate-binding pocket of SHMT2 undergoes extra rigid and unfavorable changes (Krissinel and Henrick, 2007). In the structure of the SHMT2-GZ complex, a loop region from residues Asn^{410}-Gly^{423} partly covers the entrance of the folate-binding site when GZ enters the pocket of SHMT2, indicating that the entrance of the folate-binding pocket is flexible compared with the inside of the pocket. Furthermore, we also noticed that the details of the two binding sites occupied by GZ were slightly different, such as the direction and state of GZ in the pocket (Figures 6D and 6E). This phenomenon may indicate that the hydrophobic folate-binding pocket of SHMT2 needs extra hydrogen bonds to enhance SHMT2-GZ interaction. The structure of the SHMT2-GZ complex helped us obtain deep insights into the binding model of GA with SHMT2. More importantly, based on the structural information, we have demonstrated that the carboxylic group of GA is a potential position for designing GA derivatives with improved inhibitory potency. Several GA derivatives including GEN, GPN and GBN, have been obtained. We speculate that more potent GA derivatives will be obtained if more suitable structures are anchored to the position of the GA carboxylic group.

"One drug, one target" is an expected model for drug discovery. However, a single molecule, even FDA (Food and Drug Administration)-approved single-target drug, always hits multiple different targets in real examples (MacDonald et al., 2006). Highly similar cell phenotypes and molecular features were observed in GA-treated cells and SHMT2 KO cells, indicating that SHMT2 is a critical target of GA. However, based on the observation that not all phenotypes induced by GA treatment could be fully rescued by overexpressing SHMT2, we assume that GA may still have some other unknown targets. For example, formate treatment in SHMT2 KO cells rescue cell numbers back to the level of the WT, whereas formate does not do the same in WT + GA cells (Figure 4F), which indicated that in addition to SHMT2, GA may also exert biological functions through other targets. The classical antifolate, such as PTX or LTX, inhibits several folate-dependent enzymes, and is known as multi-targeted agents. Because of the non-specific inhibition of those folate-dependent enzymes in the liver, LTX (or PTX) showed obvious toxic sideeffects in anticancer therapy(Assaraf, 2007). As indicated by Figures 6B and 6C, both triterpenoid aglycone of GZ (similar structure of GA) and antifolates (such as LTX and PTX) bind SHMT2 in close to the THF binding site, and they showed comparable binding affinities. Therefore, whether GA inhibits other folate-dependent enzymes remains as an open question. It is readily apparent that LTX and PTX are structural analogues of folic acid (Figure S8B), with a large number of polar functional groups (i.e., -NH,-NH2, -COOH groups), whereas GA is a typical hydrophobic pentacyclic triterpenoid. In terms of interaction manners, interactions between LTX (or PTX) and SHMT2 are mostly depended on the hydrogen bond (Scaletti et al., 2019),

whereas those in GA and SHMT2 are based on the hydrophobic interactions (Figures 6D and 6E). In addition, unlike the liver damaged LTX (or PTX), GA showed apparent anti-inflammatory and hepatoprotective effects. In summary, GA exhibits substantial differences with classical antifolates (LTX or PTX) in chemical structure, interaction manners with proteins, and biological functions. Therefore, we assume that GA may not act in the same way as those classical antifolates on the non-specific inhibition of those folate-dependent enzymes in the liver. Nevertheless, further investigations are still needed to reveal the potential toxicity of GA in cancer treatment.

Limitations of the study

SHMT catalyzes the reversible conversion of serine and THF into glycine and 5,10-CH_2-THF. SHMT1 is structurally similar to mitochondrial SHMT2 but localizes in the cytosol (Appaji Rao et al., 2003; Garrow et al., 1993; MacFarlane et al., 2008). Both of them play a pivotal role in one-carbon metabolism. Our preliminary SPR results indicated that GA and SHMT1 have similar binding affinity (K_D = 2.372 μM) to that of GA and SHMT2 (K_D = 2.9 μM) (Figures 3B and S8C). However, SHMT1 failed to be characterized by MS in the pull-down assays, probably because the intensity of SHMT2 exceeds that of SHMT1 by almost an order of magnitude based on the proteomic data (Figure S8D), making the binding of SHMT1 to GA more difficult. Therefore, whether GA inhibits the activity of SHMT1 or exhibits selectively inhibitory on SHMT2 *in vivo* remains an open question. Moreover, further evaluation of other target candidates of GA identified in our chemical proteomics is ongoing.

STAR★METHODS

Detailed methods are provided in the online version of this paper and include the following:

- KEY RESOURCES TABLE
- RESOURCE AVAILABILITY
  - Lead contact
  - Materials availability
  - Data and code availability
- EXPERIMENTAL MODEL AND SUBJECT DETAILS
  - Cell culture
- METHOD DETAILS
  - ShRNA knockdown cell pool construction
  - CRISPR–Cas9 knockout
  - Cell viability
  - Proliferation assays
  - Measurements of $\Delta\Psi m$
  - Measurements of ROS and NAD^+/NADH
  - Oxygen consumption
  - Protein lysate preparation
  - Sample preparation for proteomic analysis
  - Preparation of PALC agarose beads
  - Preparation and verification of GA probe
  - Pull-down experiment
  - LC–MS/MS detection
  - Metabolomics
  - Transcriptomics
  - Retro-pull-down experiment
  - Recombinant human SHMT2 expression and purification
  - Cellular thermal shift assay
  - SPR analysis
  - Fluorescence quenching assay
  - Purine and pyrimidine derivatives analysis
  - LC/MS for GA, purine and pyrimidine quantification
  - Cellular apoptosis assays
  - Crystallization, data collection and model building
  - Inhibition assay of SHMT2 using compounds
  - Synthesis of GA derivatives

SUPPLEMENTAL INFORMATION

Supplemental information can be found online at https://doi.org/10.1016/j.isci.2022.104349.

ACKNOWLEDGMENTS

This work was supported by the National Key R&D Program of China (No. 2018YFC2000305, 2018YFC1312301 and 2017YFA0505903), the National Natural Science Foundation of China (No. 82004001, 81570060, 31870826, 31670737, 81560569), the National Clinical Research Center for Geriatrics of West China Hospital at Sichuan University (No. Z20191001 and Z20191002), the West China Hospital 135 project (No. ZYYC20007), and the Sichuan Science & Technology Program (2019JDTD0013).

AUTHOR CONTRIBUTIONS

L.D. and D.S. designed the experiments and wrote the paper. X.J. involved in all experiments. L.L., Q.P. and W.P. were responsible for structure biology and *in vitro* assays; Y.P., B.D., C.G., D.S. and S.T. constructed the knockdown and knockout cell lines and gave many helpful suggestions; S.H. and L.G. participated in synthesizing the chemical probes and performed the pull-down experiments and bioinformatics analysis. Y.G., X.L., M.G. and Y.Y. performed the MS analysis. G.W., S.Q., H.X., H.H., H.Z., and P.L. provided technical assistance.

DECLARATION OF INTERESTS

The authors declare no competing interests.

Received: February 10, 2022
Revised: April 6, 2022
Accepted: April 28, 2022
Published: May 20, 2022

REFERENCES

Aly, A.M., Al-Alousi, L., and Salem, H.A. (2005). Licorice: a possible anti-inflammatory and anti-ulcer drug. AAPS PharmSciTech *6*, E74–E82. https://doi.org/10.1208/pt060113.

Appaji Rao, N., Ambili, M., Jala, V.R., Subramanya, H.S., and Savithri, H.S. (2003). Structure-function relationship in serine hydroxymethyltransferase. Biochim. Biophys.Acta *1647*, 24–29. https://doi.org/10.1016/s1570-9639(03)00043-8.

Ashton, T.M., McKenna, W.G., Kunz-Schughart, L.A., and Higgins, G.S. (2018). Oxidative phosphorylation as an emerging target in cancer therapy. Clin. Cancer Res. *24*, 2482–2490. https://doi.org/10.1158/1078-0432.ccr-17-3070.

Assaraf, Y.G. (2007). Molecular basis of antifolate resistance. Cancer Metastasis Rev. *26*, 153–181. https://doi.org/10.1007/s10555-007-9049-z.

Balsa, E., Perry, E.A., Bennett, C.F., Jedrychowski, M., Gygi, S.P., Doench, J.G., and Puigserver, P. (2020). Defective NADPH production in mitochondrial disease complex I causes inflammation and cell death. Nat. Commun. *11*, 2714. https://doi.org/10.1038/s41467-020-16423-1.

Butler, L.M., Perone, Y., Dehairs, J., Lupien, L.E., de Laat, V., Talebi, A., Loda, M., Kinlaw, W.B., and Swinnen, J.V. (2020). Lipids and cancer: emerging roles in pathogenesis, diagnosis and therapeutic intervention. Adv. Drug Deliv. Rev. *159*, 245–293. https://doi.org/10.1016/j.addr.2020.07.013.

Cai, H., Chen, X., Zhang, J., and Wang, J. (2018). 18β-glycyrrhetinic acid inhibits migration and invasion of human gastric cancer cells via the ROS/PKC-α/ERK pathway. J. Nat. Med. *72*, 252–259. https://doi.org/10.1007/s11418-017-1145-y.

Caro, P., Kishan, A.U., Norberg, E., Stanley, I.A., Chapuy, B., Ficarro, S.B., Polak, K., Tondera, D., Gounarides, J., Yin, H., et al. (2012). Metabolic signatures uncover distinct targets in molecular subsets of diffuse large B cell lymphoma. Cancer Cell *22*, 547–560. https://doi.org/10.1016/j.ccr.2012.08.014.

Cox, J., and Mann, M. (2008). MaxQuant enables high peptide identification rates, individualized p.p.b.-range mass accuracies and proteome-wide protein quantification. Nat. Biotechnol. *26*, 1367–1372. https://doi.org/10.1038/nbt.1511.

Cravatt, B.F., Wright, A.T., and Kozarich, J.W. (2008). Activity-based protein profiling: from enzyme chemistry to proteomic chemistry. Annu. Rev. Biochem. *77*, 383–414. https://doi.org/10.1146/annurev.biochem.75.101304.124125.

Currie, E., Schulze, A., Zechner, R., Walther, T.C., and Farese, R.V., Jr. (2013). Cellular fatty acid metabolism and cancer. Cell Metab. *18*, 153–161. https://doi.org/10.1016/j.cmet.2013.05.017.

Cuthbertson, C.R., Arabzada, Z., Bankhead, A., 3rd, Kyani, A., and Neamati, N. (2021). A review of small-molecule inhibitors of one-carbon enzymes: SHMT2 and MTHFD2 in the spotlight. ACS Pharmacol. Transl. Sci. *4*, 624–646. https://doi.org/10.1021/acsptsci.0c00223.

Ding, J., Li, T., Wang, X., Zhao, E., Choi, J.H., Yang, L., Zha, Y., Dong, Z., Huang, S., Asara, J.M., et al. (2013). The histone H3 methyltransferase G9A epigenetically activates the serine-glycine synthesis pathway to sustain cancer cell survival

and proliferation. Cell Metab. *18*, 896–907. https://doi.org/10.1016/j.cmet.2013.11.004.

Eaton, S. (2002). Control of mitochondrial beta-oxidation flux. Prog. Lipid Res. *41*, 197–239. https://doi.org/10.1016/s0163-7827(01)00024-8.

Farooqui, A., Khan, F., Khan, I., and Ansari, I.A. (2018). Glycyrrhizin induces reactive oxygen species-dependent apoptosis and cell cycle arrest at G(0)/G(1) in HPV18(+) human cervical cancer HeLa cell line. Biomed. Pharmacother. *97*, 752–764. https://doi.org/10.1016/j.biopha.2017.10.147.

Fulda, S., Galluzzi, L., and Kroemer, G. (2010). Targeting mitochondria for cancer therapy. Nat. Rev. Drug Discov. *9*, 447–464. https://doi.org/10.1038/nrd3137.

Garrow, T.A., Brenner, A.A., Whitehead, V.M., Chen, X.N., Duncan, R.G., Korenberg, J.R., and Shane, B. (1993). Cloning of human cDNAs encoding mitochondrial and cytosolic serine hydroxymethyltransferases and chromosomal localization. J. Biol. Chem. *268*, 11910–11916. https://doi.org/10.1016/s0021-9258(19)50286-1.

Grüner, B.M., Schulze, C.J., Yang, D., Ogasawara, D., Dix, M.M., Rogers, Z.N., Chuang, C.H., McFarland, C.D., Chiou, S.H., Brown, J.M., et al. (2016). An in vivo multiplexed small-molecule screening platform. Nat. Methods *13*, 883–889. https://doi.org/10.1038/nmeth.3992.

Haq, R., Shoag, J., Andreu-Perez, P., Yokoyama, S., Edelman, H., Rowe, G.C., Frederick, D.T., Hurley, A.D., Nellore, A., Kung, A.L., et al. (2013). Oncogenic BRAF regulates oxidative metabolism via PGC1α and MITF. Cancer Cell *23*, 302–315. https://doi.org/10.1016/j.ccr.2013.02.003.

Houten, S.M., Violante, S., Ventura, F.V., and Wanders, R.J. (2016). The biochemistry and physiology of mitochondrial fatty acid β-oxidation and its genetic disorders. Annu. Rev. Physiol. *78*, 23–44. https://doi.org/10.1146/annurev-physiol-021115-105045.

Huang, D.W., Sherman, B.T., and Lempicki, R.A. (2009). Systematic and integrative analysis of large gene lists using DAVID bioinformatics resources. Nat. Protoc. *4*, 44–57. https://doi.org/10.1038/nprot.2008.211.

Huang, L.R., Hao, X.J., Li, Q.J., Wang, D.P., Zhang, J.X., Luo, H., and Yang, X.S. (2016). 18β-Glycyrrhetinic acid derivatives possessing a trihydroxylated A ring are potent gram-positive antibacterial agents. J. Nat. Prod. *79*, 721–731. https://doi.org/10.1021/acs.jnatprod.5b00641.

Huang, R.Y., Chu, Y.L., Huang, Q.C., Chen, X.M., Jiang, Z.B., Zhang, X., and Zeng, X. (2014). 18β-Glycyrrhetinic acid suppresses cell proliferation through inhibiting thromboxane synthase in non-small cell lung cancer. PLoS One *9*, e93690. https://doi.org/10.1371/journal.pone.0093690.

Huber, K.V.M., and Superti-Furga, G. (2016). Profiling of small molecules by chemical proteomics. Methods Mol. Biol. *1394*, 211–218. https://doi.org/10.1007/978-1-4939-3341-9_15.

Ishida, T., Miki, I., Tanahashi, T., Yagi, S., Kondo, Y., Inoue, J., Kawauchi, S., Nishiumi, S., Yoshida, M., Maeda, H., et al. (2013). Effect of 18β-glycyrrhetinic acid and hydroxypropyl γcyclodextrin complex on indomethacin-induced small intestinal injury in mice. Eur. J. Pharmacol. *714*, 125–131. https://doi.org/10.1016/j.ejphar.2013.06.007.

Jeong, H.G., You, H.J., Park, S.J., Moon, A.R., Chung, Y.C., Kang, S.K., and Chun, H.K. (2002). Hepatoprotective effects of 18β-glycyrrhetinic acid on carbon tetrachloride-induced liver injury: inhibition of cytochrome P450 2E1 expression. Pharmacol. Res. *46*, 221–227. https://doi.org/10.1016/s1043-6618(02)00121-4.

Jinek, M., Jiang, F., Taylor, D.W., Sternberg, S.H., Kaya, E., Ma, E., Anders, C., Hauer, M., Zhou, K., Lin, S., et al. (2014). Structures of Cas9 endonucleases reveal RNA-mediated conformational activation. Science *343*, 1247997. https://doi.org/10.1126/science.1247997.

Jones, R.A., Robinson, T.J., Liu, J.C., Shrestha, M., Voisin, V., Ju, Y., Chung, P.E., Pellecchia, G., Fell, V.L., Bae, S., et al. (2016). RB1 deficiency in triple-negative breast cancer induces mitochondrial protein translation. J. Clin. Invest. *126*, 3739–3757. https://doi.org/10.1172/jci81568.

Kim, D., Fiske, B.P., Birsoy, K., Freinkman, E., Kami, K., Possemato, R.L., Chudnovsky, Y., Pacold, M.E., Chen, W.W., Cantor, J.R., et al. (2015). SHMT2 drives glioma cell survival in ischaemia but imposes a dependence on glycine clearance. Nature *520*, 363–367. https://doi.org/10.1038/nature14363.

Kim, Y.H., Kim, D.E., and Lee, S.H. (2018). Effects of 18β-glycyrrhetinic acid on fungal protease-induced airway inflammatory responses. Mediators Inflamm. *2018*, 6461032. https://doi.org/10.1155/2018/6461032.

Krissinel, E., and Henrick, K. (2007). Inference of macromolecular assemblies from crystalline state. J. Mol. Biol. *372*, 774–797. https://doi.org/10.1016/j.jmb.2007.05.022.

Li, J., Tang, F., Li, R., Chen, Z., Lee, S.M.Y., Fu, C., Zhang, J., and Leung, G.P.H. (2020). Dietary compound glycyrrhetinic acid suppresses tumor angiogenesis and growth by modulating antiangiogenic and proapoptotic pathways *in vitro* and *in vivo*. J. Nutr. Biochem. *77*, 108268. https://doi.org/10.1016/j.jnutbio.2019.108268.

Li, X., Sun, R., and Liu, R. (2019). Natural products in licorice for the therapy of liver diseases: progress and future opportunities. Pharmacol. Res. *144*, 210–226. https://doi.org/10.1016/j.phrs.2019.04.025.

Li, Z., and Zhang, H. (2016). Reprogramming of glucose, fatty acid and amino acid metabolism for cancer progression. Cell Mol. Life Sci. *73*, 377–392. https://doi.org/10.1007/s00018-015-2070-4.

Liu, C., Wang, L., Liu, X., Tan, Y., Tao, L., Xiao, Y., Deng, P., Wang, H., Deng, Q., Lin, Y., et al. (2021). Cytoplasmic SHMT2 drives the progression and metastasis of colorectal cancer by inhibiting β-catenin degradation. Theranostics *11*, 2966–2986. https://doi.org/10.7150/thno.48699.

Lucas, S., Chen, G., Aras, S., and Wang, J. (2018). Serine catabolism is essential to maintain mitochondrial respiration in mammalian cells. Life Sci. Alliance *1*, e201800036. https://doi.org/10.26508/lsa.201800036.

MacDonald, M.L., Lamerdin, J., Owens, S., Keon, B.H., Bilter, G.K., Shang, Z., Huang, Z., Yu, H., Dias, J., Minami, T., et al. (2006). Identifying off-target effects and hidden phenotypes of drugs in human cells. Nat. Chem. Biol. *2*, 329–337. https://doi.org/10.1038/nchembio790.

MacFarlane, A.J., Liu, X., Perry, C.A., Flodby, P., Allen, R.H., Stabler, S.P., and Stover, P.J. (2008). Cytoplasmic serine hydroxymethyltransferase regulates the metabolic partitioning of methylenetetrahydrofolate but is not essential in mice. J. Biol. Chem. *283*, 25846–25853. https://doi.org/10.1074/jbc.m802671200.

Maddocks, O.D.K., Labuschagne, C.F., Adams, P.D., and Vousden, K.H. (2016). Serine metabolism supports the methionine cycle and DNA/RNA methylation through de novo ATP synthesis in cancer cells. Mol. Cell *61*, 210–221. https://doi.org/10.1016/j.molcel.2015.12.014.

Martínez-Reyes, I., and Chandel, N.S. (2021). Cancer metabolism: looking forward. Nat. Rev. Cancer *21*, 669–680. https://doi.org/10.1038/s41568-021-00378-6.

Minton, D.R., Nam, M., McLaughlin, D.J., Shin, J., Bayraktar, E.C., Alvarez, S.W., Sviderskiy, V.O., Papagiannakopoulos, T., Sabatini, D.M., Birsoy, K., and Possemato, R. (2018). Serine catabolism by SHMT2 is required for proper mitochondrial translation initiation and maintenance of formylmethionyl-tRNAs. Mol. Cell *69*, 610–621.e5. https://doi.org/10.1016/j.molcel.2018.01.024.

Morscher, R.J., Ducker, G.S., Li, S.H.J., Mayer, J.A., Gitai, Z., Sperl, W., and Rabinowitz, J.D. (2018). Mitochondrial translation requires folate-dependent tRNA methylation. Nature *554*, 128–132. https://doi.org/10.1038/nature25460.

Murphy, M.P., and Hartley, R.C. (2018). Mitochondria as a therapeutic target for common pathologies. Nat. Rev. Drug Discov. *17*, 865–886. https://doi.org/10.1038/nrd.2018.174.

Neggers, J.E., Kwanten, B., Dierckx, T., Noguchi, H., Voet, A., Bral, L., Minner, K., Massant, B., Kint, N., Delforge, M., et al. (2018). Target identification of small molecules using large-scale CRISPR-Cas mutagenesis scanning of essential genes. Nat. Commun. *9*, 502. https://doi.org/10.1038/s41467-017-02349-8.

Newman, D.J., and Cragg, G.M. (2016). Natural products as sources of new drugs from 1981 to 2014. J. Nat. Prod. *79*, 629–661. https://doi.org/10.1021/acs.jnatprod.5b01055.

Nguyen, T.H., Vemu, P.L., Hoy, G.E., Boudjadi, S., Chatterjee, B., Shern, J.F., Khan, J., Sun, W., and Barr, F.G. (2021). Serine hydroxymethyltransferase 2 expression promotes tumorigenesis in rhabdomyosarcoma with 12q13-14 amplification. J. Clin. Invest. *131*, e138022.

Porporato, P.E., Filigheddu, N., Pedro, J.M.B.S., Kroemer, G., and Galluzzi, L. (2018). Mitochondrial metabolism and cancer. Cell Res. *28*, 265–280. https://doi.org/10.1038/cr.2017.155.

Satomi, Y., Nishino, H., and Shibata, S. (2005). Glycyrrhetinic acid and related compounds induce G1 arrest and apoptosis in human hepatocellular carcinoma HepG2. Anticancer Res. *25*, 4043–4047.

Scaletti, E., Jemth, A.S., Helleday, T., and Stenmark, P. (2019). Structural basis of inhibition of the human serine hydroxymethyltransferase SHMT2 by antifolate drugs. FEBS Lett. *593*, 1863–1873. https://doi.org/10.1002/1873-3468.13455.

Schenone, M., Dančík, V., Wagner, B.K., and Clemons, P.A. (2013). Target identification and mechanism of action in chemical biology and drug discovery. Nat. Chem. Biol. *9*, 232–240. https://doi.org/10.1038/nchembio.1199.

Schooneman, M.G., Vaz, F.M., Houten, S.M., and Soeters, M.R. (2013). Acylcarnitines: reflecting or inflicting insulin resistance? Diabetes *62*, 1–8. https://doi.org/10.2337/db12-0466.

Schwarz, S., Lucas, S.D., Sommerwerk, S., and Csuk, R. (2014). Amino derivatives of glycyrrhetinic acid as potential inhibitors of cholinesterases. Bioorg. Med. Chem. *22*, 3370–3378. https://doi.org/10.1016/j.bmc.2014.04.046.

Shackelford, D.B., Abt, E., Gerken, L., Vasquez, D.S., Seki, A., Leblanc, M., Wei, L., Fishbein, M.C., Czernin, J., Mischel, P.S., and Shaw, R. (2013). LKB1 inactivation dictates therapeutic response of non-small cell lung cancer to the metabolism drug phenformin. Cancer Cell *23*, 143–158. https://doi.org/10.1016/j.ccr.2012.12.008.

Shen, S., Zhou, M., Huang, K., Wu, Y., Ma, Y., Wang, J., Ma, J., and Fan, S. (2017). Blocking autophagy enhances the apoptotic effect of 18β-glycyrrhetinic acid on human sarcoma cells via endoplasmic reticulum stress and JNK activation. Cell Death Dis. *8*, e3055. https://doi.org/10.1038/cddis.2017.441.

Song, J., Ko, H.S., Sohn, E.J., Kim, B., Kim, J.H., Kim, H.J., Kim, C., Kim, J.E., and Kim, S.H. (2014). Inhibition of protein kinase C α/βII and activation of c-Jun NH2-terminal kinase mediate glycyrrhetinic acid induced apoptosis in non-small cell lung cancer NCI-H460 cells. Bioorg. Med. Chem. Lett. *24*, 1188–1191. https://doi.org/10.1016/j.bmcl.2013.12.111.

Subramanian, A., Tamayo, P., Mootha, V.K., Mukherjee, S., Ebert, B.L., Gillette, M.A., Paulovich, A., Pomeroy, S.L., Golub, T.R., Lander, E.S., and Mesirov, J.P. (2005). Gene set enrichment analysis: a knowledge-based approach for interpreting genome-wide expression profiles. Proc. Natl. Acad. Sci. U S A *102*, 15545–15550. https://doi.org/10.1073/pnas.0506580102.

Tani, H., Mito, T., Velagapudi, V., Ishikawa, K., Umehara, M., Nakada, K., Suomalainen, A., and Hayashi, J.I. (2019). Disruption of the mouse Shmt2 gene confers embryonic anaemia via foetal liver-specific metabolomic disorders. Sci. Rep. *9*, 16054. https://doi.org/10.1038/s41598-019-52372-6.

Tani, H., Ohnishi, S., Shitara, H., Mito, T., Yamaguchi, M., Yonekawa, H., Hashizume, O., Ishikawa, K., Nakada, K., and Hayashi, J.I. (2018). Mice deficient in the Shmt2 gene have mitochondrial respiration defects and are embryonic lethal. Sci. Rep. *8*, 425. https://doi.org/10.1038/s41598-017-18828-3.

Tedeschi, P.M., Markert, E.K., Gounder, M., Lin, H., Dvorzhinski, D., Dolfi, S.C., Chan, L.L.Y., Qiu, J., DiPaola, R.S., Hirshfield, K.M., et al. (2013). Contribution of serine, folate and glycine metabolism to the ATP, NADPH and purine requirements of cancer cells. Cell Death Dis. *4*, e877. https://doi.org/10.1038/cddis.2013.393.

Tibbetts, A.S., and Appling, D.R. (2010). Compartmentalization of Mammalian folate-mediated one-carbon metabolism. Annu. Rev. Nutr. *30*, 57–81. https://doi.org/10.1146/annurev.nutr.012809.104810.

Titov, D.V., Gilman, B., He, Q.L., Bhat, S., Low, W.K., Dang, Y., Smeaton, M., Demain, A.L., Miller, P.S., Kugel, J.F., et al. (2011). XPB, a subunit of TFIIH, is a target of the natural product triptolide. Nat. Chem. Biol. *7*, 182–188. https://doi.org/10.1038/nchembio.522.

Viale, A., Pettazzoni, P., Lyssiotis, C.A., Ying, H., Sánchez, N., Marchesini, M., Carugo, A., Green, T., Seth, S., Giuliani, V., et al. (2014). Oncogene ablation-resistant pancreatic cancer cells depend on mitochondrial function. Nature *514*, 628–632. https://doi.org/10.1038/nature13611.

Wang, L.J., Geng, C.A., Ma, Y.B., Huang, X.Y., Luo, J., Chen, H., Zhang, X.M., and Chen, J.J. (2012). Synthesis, biological evaluation and structure-activity relationships of glycyrrhetinic acid derivatives as novel anti-hepatitis B virus agents. Bioorg. Med. Chem. Lett. *22*, 3473–3479. https://doi.org/10.1016/j.bmcl.2012.03.081.

Wang, S., Shen, Y., Qiu, R., Chen, Z., Chen, Z., and Chen, W. (2017). 18 beta-glycyrrhetinic acid exhibits potent antitumor effects against colorectal cancer via inhibition of cell proliferation and migration. Int. J. Oncol. *51*, 615–624. https://doi.org/10.3892/ijo.2017.4059.

Wang, W., Karamanlidis, G., and Tian, R. (2016). Novel targets for mitochondrial medicine. Sci. Transl. Med. *8*, 326rv323. https://doi.org/10.1126/scitranslmed.aac7410.

Wang, X.F., Zhou, Q.M., Lu, Y.Y., Zhang, H., Huang, S., and Su, S.B. (2015). Glycyrrhetinic acid potently suppresses breast cancer invasion and metastasis by impairing the p38 MAPK-AP1 signaling axis. Expert Opin. Ther. Targets *19*, 577–587. https://doi.org/10.1517/14728222.2015.1012156.

Wei, Z., Song, J., Wang, G., Cui, X., Zheng, J., Tang, Y., Chen, X., Li, J., Cui, L., Liu, C.Y., and Yu, W. (2018). Deacetylation of serine hydroxymethyltransferase 2 by SIRT3 promotes colorectal carcinogenesis. Nat. Commun. *9*, 4468. https://doi.org/10.1038/s41467-018-06812-y.

Weinberg, S.E., and Chandel, N.S. (2015). Targeting mitochondria metabolism for cancer therapy. Nat. Chem. Biol. *11*, 9–15. https://doi.org/10.1038/nchembio.1712.

Xu, R.H., Pelicano, H., Zhou, Y., Carew, J.S., Feng, L., Bhalla, K.N., Keating, M.J., and Huang, P. (2005). Inhibition of glycolysis in cancer cells: a novel strategy to overcome drug resistance associated with mitochondrial respiratory defect and hypoxia. Cancer Res. *65*, 613–621.

Xu, Y., Xue, D., Bankhead, A., 3rd, and Neamati, N. (2020). Why all the fuss about oxidative phosphorylation (OXPHOS)? J. Med. Chem. *63*, 14276–14307. https://doi.org/10.1021/acs.jmedchem.0c01013.

Yang, L., Garcia Canaveras, J.C., Chen, Z., Wang, L., Liang, L., Jang, C., Mayr, J.A., Zhang, Z., Ghergurovich, J.M., Zhan, L., et al. (2020). Serine catabolism feeds NADH when respiration is impaired. Cell Metab. *31*, 809–821.e6. https://doi.org/10.1016/j.cmet.2020.02.017.

Yang, X., Wang, Z., Li, X., Liu, B., Liu, M., Liu, L., Chen, S., Ren, M., Wang, Y., Yu, M., et al. (2018). SHMT2 desuccinylation by SIRT5 drives cancer cell proliferation. Cancer Res. *78*, 372–386. https://doi.org/10.1158/0008-5472.can-17-1912.

Ye, J., Fan, J., Venneti, S., Wan, Y.W., Pawel, B.R., Zhang, J., Finley, L.W., Lu, C., Lindsten, T., Cross, J.R., et al. (2014). Serine catabolism regulates mitochondrial redox control during hypoxia. Cancer Discov. *4*, 1406–1417. https://doi.org/10.1158/2159-8290.cd-14-0250.

Zhang, C., Liu, Z., Zheng, Y., Geng, Y., Han, C., Shi, Y., Sun, H., Zhang, C., Chen, Y., Zhang, L., et al. (2018). Glycyrrhetinic acid functionalized graphene oxide for mitochondria targeting and cancer treatment in vivo. Small *14*, 1703306. https://doi.org/10.1002/smll.201703306.

Zhou, Y., Zhou, B., Pache, L., Chang, M., Khodabakhshi, A.H., Tanaseichuk, O., Benner, C., and Chanda, S.K. (2019). Metascape provides a biologist-oriented resource for the analysis of systems-level datasets. Nat. Commun. *10*, 1523. https://doi.org/10.1038/s41467-019-09234-6.

STAR★METHODS

KEY RESOURCES TABLE

REAGENT or RESOURCE	SOURCE	IDENTIFIER
Antibodies		
Rabbit monoclonal anti-SHMT2	Novogene	Cat#NHA3260
Rabbit monoclonal anti-NDUFS1	Abcam	Cat#ab169540; RID:AB_2687932
Rabbit monoclonal anti-NDUFA9	Novogene	Cat#NHA15622
Rabbit monoclonal anti-NDUFB8	Huabio(http://www.huabio.cn/)	Cat#ET7108-25
Rabbit polyclonal anti-SDHA	Huabio(http://www.huabio.cn/)	Cat#ET1703-40
Rabbit monoclonal anti-SDHB	Huabio(http://www.huabio.cn/)	Cat#ER1803-63
Mouse monoclonal anti-β-Actin	Huabio(http://www.huabio.cn/)	Cat#EM21002
Rabbit polyclonal anti-MT-ND1	Novogene	Cat#NHA2255
Mouse monoclonal anti-Flag	Huabio(http://www.huabio.cn/)	Cat#ET1703-40
Rabbit monoclonal anti-GAPDH	Huabio(http://www.huabio.cn/)	Cat#ET1601-4
Rabbit monoclonal anti-MT-CO1	Abcam	Cat#ab203912; RRID:AB_2801537
Rabbit polyclonal anti-MT-CO2	Proteintech	Cat#55070-1-AP; RRID:AB_10859832
Rabbit monoclonal anti-CPOX	ABclonal	Cat#A3807; RRID:AB_2765315
Bacterial and virus strains		
pLVX-IRES-Puro plasmid	Takara	Cat#632183;
Viral packaging plasmids psPAX2	Addgene	Cat#12260 RRID:Addgene_12260
Viral packaging plasmids pMD2.G	Addgene	Cat#12259; RRID:Addgene_12259
pETDuet-1 vector	Novagen	Cat#71146
Chemicals, peptides, and recombinant proteins		
Tetrahydrofolic acid (THF)	Ark Pharm	Cat#RQL910
18β-glycyrrhetinic acid (GA)	Biopurify, Chengdu, China	Cat#BP0681
Carbenoxolone disodium (CBX)	Sigma-Aldrich	Cat#C4790
Glycyrrhizic acid (GZ)	Biopurify, Chengdu, China	Cat#BP0682
DMEM/high glucose medium	Gibco	Cat#C11995-065
Fetal bovine serum (FBS)	NATOCOR	Cat#SFBE
Penicillin and streptomycin	Gibco	Cat#15140–122
RPMI-1640	Gibco	Cat#11875-093
Lipo2000	Thermo Fisher Scientific	Cat#11668027
Polyethylene	Sigma–Aldrich	Cat#P1458
3-(4,5-dimethylthiazol-2-yl)-2,5-diphenyl tetrazolium bromide (MTT)	Sigma–Aldrich	Cat#475989
Sodium formate	Sigma–Aldrich	Cat#112682
Complete protease inhibitor	Bimake	Cat#B14002
Phosphatase inhibitor cocktails A and B	Bimake	Cat#B15002
Tetraethylammonium bromide	Sigma–Aldrich	Cat#15715-58-9
Tris(2-carboxyethyl)phosphine)	Sigma–Aldrich	Cat#C4706
Iodoacetamide	Sigma–Aldrich	Cat#I1149
Trypsin	Progema	Cat#V5117
Pyridoxal 5′-phosphate hydrate (PLP)	Sigma–Aldrich	Cat#P9255
4-[3-(Trifluoromethyl)-3H-diazirin-3-yl] benzoic acid	TCI (www.tcichemicals.com/CN/zh/)	Cat#T2820

(*Continued on next page*)

Continued

REAGENT or RESOURCE	SOURCE	IDENTIFIER
1-hydroxybenzotriazole (HOBT)	J&K Scientific	Cat#517257
N-(3-Dimethylaminopropyl)-N′-Ethylcarbodiimide Hydrochloride (EDCI)	MACKLIN	Cat#N835594
N,N-Diisopropylethylamine (DIPEA)	MACKLIN	Cat#N807281
Critical commercial assays		
Mitochondrial Membrane Potential Assay Kit with JC-1	Beyotime Biotechnology	Cat#C2006
Reactive Oxygen Species Assay Kit	Beyotime Biotechnology	Cat#S0033
NAD^+/NADH Assay Kit	Beyotime Biotechnology	Cat#S0175
Agilent Seahorse XF Cell Mito Stress Test Kit	Agilent Seahorse	Cat#103015-100
7-AAD Apoptosis Detection Kit	BioLegend	Cat#640930
Bradford assay	Bio–Rad	Cat#5000205
TMT10plex Isobaric Label Reagent Set	Thermo Fisher	Cat#90111
Deposited data		
The mass spectrometry raw data and the corresponding txt files	ProteomeXchange Consortium via the iProX partner repository (http://proteomecentral.proteomexchange.org)	PXD031021
Protein Data Bank	https://www.rcsb.org/	7BYH
Other Original Data	https://data.mendeley.com/drafts/82gydtyy82	https://doi.org/10.17632/82gydtyy82.1
Experimental models: Cell lines		
Human cervical cancer cell line, HeLa	National Infrastructure of Cell Line Resource (Beijing, China)	http://medportal.bmicc.cn/
Human colorectal carcinoma, HCT116	National Infrastructure of Cell Line Resource (Beijing, China)	http://medportal.bmicc.cn/
Human melanoma cell line, A375	National Infrastructure of Cell Line Resource (Beijing, China)	http://medportal.bmicc.cn/
Human hepatoma cell line, HepG2	National Infrastructure of Cell Line Resource (Beijing, China)	http://medportal.bmicc.cn/
Human lung cancer cell line, A549	National Infrastructure of Cell Line Resource (Beijing, China)	http://medportal.bmicc.cn/
Human osteosarcoma cell line, U2OS	National Infrastructure of Cell Line Resource (Beijing, China)	http://medportal.bmicc.cn/
Human embryonic kidney cell line, HEK293T	National Infrastructure of Cell Line Resource (Beijing, China)	http://medportal.bmicc.cn/
Experimental models: Organisms/strains		
Mouse: Balb/c nude, (male, 6 weeks)	Beijing Huafukang Biosciences Co. Inc.	N/A
Oligonucleotides		
SHMT2-shRNA primers:Forward:CCGGCG GAGAGTTGTGGACTTTATACTCGAGTAT AAAGTCCACAACTCTCCGTTTTTT. Reverse:AATTAAAAAACGGAGAGTTGTG GACTTTATACTCGAGTATAAAGTCCACA ACTCTCCG.	This paper	N/A
The guide sequences targeting exon 2 of human SHMT2 were sgSHMT2-1: 5'-GGA CAGGCAGTGTCGTGGCC-3' and sgSHMT 2-2: 5'-GCTCAGGATCACTGTCCGAC-3'.	This paper	N/A

(*Continued on next page*)

Continued

REAGENT or RESOURCE	SOURCE	IDENTIFIER
The guide sequence of human CPOX was sgCPOX: 5'-GGGCACGGCTCGACGTCGAG-3'.	This paper	N/A
Software and algorithms		
A Gene Annotation & Analysis Resource (Metascape)	Zhou et al. (2019)	2018-11-11(Update); https://www.metascape.org
MaxQuant	Cox and Mann (2008)	Version 1.5.3; https://www.maxquant.org/
DAVID Bioinformatics Resources	Huang da et al., 2009	Version 6.8; https://david.ncifcrf.gov/
Gene Set Enrichment Analysis (GSEA)	Subramanian et al. (2005)	Version:h.all.v6.2. symbols.gmt[Hallmarks]
Human UniProt database	https://www.uniprot.org/proteomes/UP000005640	20,239 entries, (2017/09)
Human genome HG19 Reseq annotation	UCSCdatabase (http://genome.ucsc.edu/)	Genome Reference Consortium Human Build 37 patch release 13 (GRCh37.p13)
Quantitative transcripts	FEATURES COUNTS quantitative software	Release 1.6.2
GraphPad Prism	https://www.graphpad.com/scientific-software/prism/	Version: 9.0.0
RStudio	https://www.rstudio.com/	Version: 3.6.1
Other		
Ni-NTA agarose beads	QIAGEN	Cat#36111
NHS-activated Sepharose TM 4 Fast Flow beads	GE Healthcare Life Science	Cat#17090601
CM5 chips	GE Healthcare	Cat#BR-1005-30

RESOURCE AVAILABILITY

Lead contact

Further information and requests for resources and reagents should be directed to and will be fulfilled by the lead contact, Dr. Lunzhi Dai(lunzhi.dai@scu.edu.cn).

Materials availability

This study did not generate new unique reagents.

Data and code availability

Data availability

The mass spectrometry raw data and the corresponding txt files have been deposited in the ProteomeXchange Consortium (http://proteomecentral.proteomexchange.org) via the iProX partner repository with a dataset identifier of PXD031021. The atomic coordinates and structure factors have been deposited in the Protein Data Bank under accession number 7BYH (crystal structure of SHMT2-GZ complex).

Code availability

The raw data are available on Mendeley Data (https://doi.org/10.17632/82gydtyy82.1)

Any additional information required to reanalyze the data reported in this paper is available from the Lead contact upon request.

EXPERIMENTAL MODEL AND SUBJECT DETAILS

Cell culture

HeLa, HCT116, A375, HepG2, A549, U-2OS and HEK293T cell lines were obtained from the National Infrastructure of Cell Line Resource (Beijing, China). HeLa, HCT116, A375, HepG2 and U-2OS cells were cultured in DMEM/high glucose medium supplemented with 10% (v/v) FBS, 100 U/mL penicillin, and 100 μg/mL streptomycin. A549 cells were cultured in RPMI-1640 supplemented with 10% (v/v) FBS (BI), 100 U/mL penicillin, and 100 μg/mL streptomycin. All cell lines were maintained at 37°C under a humidified 5% CO_2 atmosphere according to supplier recommendations.

METHOD DETAILS

ShRNA knockdown cell pool construction

Lentiviral expression systems were used to generate overexpression and SHMT2 gene knockdown cell lines. Transfect the plasmid with shRNA targeting SHMT2 and retroviral packaging plasmid into HEK293T cells with Lipo2000, and collect the supernatant virus after 48 h. The target cells in the 6-well tissue culture plate were infected with virus medium containing 1.25 μg/mL polyethylene (4×10^5 cells per well). After 48 h, virus-infected cells were selected with 1.5 μg/mL puromycin. The SHMT2 shRNAs effectively knockdown were determined by western blot and chosen for our experiments. Empty vector (shNC) served as a negative control for gene knockdown. Similarly, we constructed overexpression cell lines.

CRISPR–Cas9 knockout

Briefly, sgRNA sequences targeting SHMT2 were designed by the CRISPR designer at http://crispr.mit.edu/.The sgRNA sequences were cloned into the pLVX-IRES-Puro plasmid, and then cotransfected with viral packaging plasmids psPAX2 and pMD2.G into HEK293T cells. Media were changed at 6 h after transfection, and the virus-containing supernatant was collected at 48 h after transfection. The supernatant was centrifuged at 13,000 g for 2 min at 4°C and then stored at −80°C or used immediately. HeLa cells were infected with the lentiviral vector at an MOI of 1 and selected with 1 μg/mL puromycin. Single cells were plated into 96-well plates by diluting the cell suspension to a concentration of 0.5-1 cells per well. Cells were grown for 2–3 weeks in 96-well plates and then expanded. Knockout of SHMT2 and CPOX in cells was confirmed by western blot.

Cell viability

Cell viability was determined using standard dark-blue formazan crystals. Briefly, approximately 3,000 cells were seeded in 96-well plates and allowed to adhere for 12 h. Then, a series of different concentrations of compound were added and incubated with the cells for another 48 h before 3-(4,5-dimethylthiazol-2-yl)-2,5-diphenyl tetrazolium bromide (MTT) was added. After 4 h, the resultant dark-blue formazan crystals were dissolved and measured by an SYNERGY microplate reader (BioTek, USA) at a wavelength of 570 nm.

Proliferation assays

For HeLa stable cells with knockout SHMT2 or wild-type, direct cell counts were carried out by plating cells in triplicate in 6-well plates at 4×10^5 cells per well in 2 mL of media containing 100μMGA (or DMSO control). Cells were counted every day over a 5-day period. For A375 cell lines (shNC or shSHMT2), cells were seeded in 12-well plates at 1.2×10^5 cells per well and counted every 12 h over 72 h. For formate treatment, 0.5 mM sodium formate was added for 3 days prior to imitating proliferation assays, and then HeLa stable cells with knockout SHMT2 or wild-type were seeded in 6-well plates at 2.5×10^5 cells per well and exposed to 100μMGA (or DMSO control) for 3 days. All cells were counted using a countstar (Countstar BioTech, China).

Measurements of $\Delta\Psi m$

$\Delta\Psi m$ was determined by a Mitochondrial Membrane Potential Assay Kit with JC-1 according to the recommended protocol. In brief, cells were seeded in 6-well plates and exposed to 100μMGA (or DMSO control) for 12 h. Then, 10 μM JC-1 was added and the cells were incubated for another 20 min. The cells were subsequently washed twice with JC-1 staining buffer and visualized under a fluorescence microscope, and the green fiuorescence signal indicated degradation of $\Delta\Psi m$.

Measurements of ROS and NAD^+/NADH

The levels of ROS and NAD^+/NADH ratios were detected by a Reactive Oxygen Species Assay Kit and NAD^+/NADH Assay Kit, respectively, according to the manufacturer's instructions. Cells were exposed to increasing concentrations of GA for 4 h before analysis.

Oxygen consumption

Oxygen consumption rates were measured by an Agilent Seahorse XF Cell Mito Stress Test Kit on an XF24 extracellular flux analyzer (Seahorse Bioscience, Chicopee, MA) following the manufacturer's instructions. Briefly, cells were seeded in XF24 cell culture microplates and exposed to 100μMGA (or DMSO control) for 12 h after reaching 80% confluency. Cells were equilibrated for 1 h in XF assay medium in a non-CO_2 incubator. Oxygen consumption rates were monitored throughout sequential injections of oligomycin (1 μM), carbonyl cyanide-4-(trifluoromethoxy)phenylhydrazone (1 μM) and rotenone/antimycin A (0.5 μM). Then cells in oxygen consumption rates measurements were harvested and counted. Data for each well were normalized to cell number.

Protein lysate preparation

Cells were washed with PBS (pH = 7.4) and lysed with RIPA buffer (1% NP-40, 0.5% (w/v) sodium deoxycholate, 150 mM NaCl, 50 mM Tris (pH = 7.5)) supplemented with complete protease inhibitor and phosphatase inhibitor cocktails A and B. Protein quantification was performed by the Bradford assay. All lysates were freshly prepared followed by western blotting or proteomic analysis.

Sample preparation for proteomic analysis

Protein lysates of wild-type HeLa cells treated with 100μMGA (or DMSO control) for 48 h and those with SHMT2 knockout (treated with NS) were prepared in triplicate. Each protein sample was diluted to 1 μg/μL (50 μg in all) with 100 mM tetraethylammonium bromide, reduced with 200 mM Tris(2-carboxyethyl) phosphine), alkylated with 375 mM iodoacetamide, precipitated with methanol, chloroform and water (CH_3OH:$CHCl_3$:H_2O = 4:1:3), and subjected to overnight digestion with trypsin (1:50 enzyme to protein ratio). The tryptic peptides were labeled with 9 plexes of TMT10 reagents according to the manufacturer's protocol. Then, the TMT-labeled peptides were mixed and fractionated by an Agilent Poroshell HPH C18 column (250 × 4.6 mm, OD 4 μm) at a flow rate of 1 mL/min on an Agilent 1260 instrument. Buffer A (2% ACN, 10 mM NH_4COOH, pH = 10) and a non-linear increasing concentration of buffer B (90% ACN, 10 mM NH_4COOH, pH = 10) were used for peptide separation. A standard 120 min gradient was used as follows: 0–8% B in 10 min; 8%–35% B in 70 min; 35%–60% B in 15 min; 60%–70% B in 10 min; and 70–100% B in 15 min. The peptide mixture was separated into 120 fractions and combined by a concatenation strategy into 30 fractions (1&31, 2&32 … 30&120). The combined fractions were used for further LC-MS/MS analysis.

Preparation of PALC agarose beads

NHS-activated agarose beads (10 mL) were pre-activated with 1 mM HCl, and washed four times with 30 mL PBS (pH = 7.4). After the liquid was drained, 20 mL 2,2′-(ethylenedioxy) bis(ethylamine) solution (1M, the linker solution) was added and incubated for 4hat room temperature. Then, the beads were washed four times with 10 mM HCl, three times with PBS (pH = 7.4), and three times with ethanol to completely remove the excess linker, and obtained the linker-linked agarose beads. At the same time, 4-[3-(Trifluoromethyl)-3H-diazirin-3-yl] benzoic acid (68 mg, 340 μmol), N-(3-Dimethylaminopropyl)-N′-Ethylcarbodiimide Hydrochloride (EDCI, 259 mg, 1.36 mmol), N-Hydroxysuccinimide, (NHS, 156 mg, 1.36 mmol) were dissolved in 3 mL acetonitrile and incubated at room temperature for 2 h in the dark. Next, the reacted 4-[3-(Trifluoromethyl)-3H-diazirin-3-yl] benzoic acid solution, 300 μL TEAB (1M) were added into the linker-linked agarose beads (4 mL) and incubate overnight at room temperature in the dark. After the reaction complete, the Photoaffinity-linker-coated (PALC) agarose beads were washed 4 times with acetonitrile, 3 times with water, and 3 times with absolute ethanol, and dispensed into brown tubes in the dark.

Preparation and verification of GA probe

PALC beads (1 mL), a mixture of PALC beads (1 mL) and GA solution (15 mg in 1 mL ethanol), or a mixture of blank beads (1 mL) and GA solution (15 mg in 1 mL ethanol) were transferred into a glass sample vial. Solvents were removed using a rotary evaporator, and beads were dried in vacuum in the dark. The dried beads were irradiated at 365 nm ($4Jcm^{-2}$) for 15 min by an ultraviolet crosslinker (LYUV07 – II, NingBo,

China), and the resulting beads were washed successively with 50% ethanol, ethanol, and methanol (3 × 400 μL each) to give a GA probe or its control. The washed solvents were collected, and the redundant GA was quantified by further LC-MS analysis. In addition, GA solid (power), GA probe (1 mL, theoretical content of GA is 16 mmol), blank beads (1 mL), and a physical mixture of GA power (16 mmol) and blank beads (1 mL) were prepared and further analyzed by a Nicolet iS10 FT-IR spectrometer (Thermo Fisher Scientific, Waltham, USA).

Pull-down experiment

HeLa cells were lysed in NETN (0.1% NP-40, 0.5 mM EDTA, 20 mM Tris-HCl, 150 mM $NaCl_2$, protease inhibitor cocktail, pH = 8.0). The extracted proteins (2 mg) were first preincubated in the presence or absence of GA (100 μM) at 4°C overnight, and then GA-immobilized beads or GA-free beads were added to each sample and incubated at 4°C for an additional 4 h. Subsequently, the beads were washed with NETN 3 times, eluted with 1×SDS-loading buffer (20 μL), and then boiled for 5 min at 95°C. The eluted proteins were analyzed in accordance with the digestion in gel method and further analyzed by LC-MS/MS with label-free quantification.

LC–MS/MS detection

The LC–MS/MS detection system consisted of a nanoflow HPLC instrument (Easy nLC1000 System) coupled to a Q Exactive Plus mass spectrometer (Thermo Fisher Scientific) with a nanoelectrospray ion source. Samples were resolved in buffer A (0.1% formic acid), loaded onto a 2-cm self-packed trap column (75-μm inner diameter) using buffer A and separated on a 75-μm-inner-diameter column with a length of 12 cm. TMT-labelled samples were separated over a 65-min gradient (buffer A,0.1% formic acid in water; buffer B, 0.1% FA in CH_3CN) or a 65-min gradient for label-free samples at a flow rate of 300 nL/min. Data-dependent acquisition was performed in positive ion mode, and a full mass spectrometry scan ranged from 350 to 1600 *m/z* at a resolution of 70,000 with a the maximum injection time of 20 ms. For MS2 scans, spectra with a charge state of one or unassigned charge states were excluded from fragmentation by higher-energy collision dissociation with a normalized collision energy of 30%. The MS2 spectra were acquired in the trap in rapid mode with an AGC target of 100,000 and a maximum injection time of 100 ms. For MS/MS scans, the top 15 most intense parent ions were selected with a 0.6 *m/z* isolation window and fragmented with a normalized collision energy (NCE) of 30%. The AGC value for MS/MS was set to a target value of 1×10^5, with a maximum injection time of 100 ms and a resolution of 35,000. Parent ions with a charge state of z = 1 or with unassigned charge states were excluded from fragmentation and the intensity threshold for selection was set to 2×10^5.

Metabolomics

HeLa stable cell lines with SHMT2 knockout or wild-type were seeded in 10 cm plates in the presence of 100μMGA (or DMSO control). After 48 h, the medium was aspirated, the cells were rinsed with 1 mL of PBS (pH = 7.4), and metabolism was quenched by adding 2 mL of dry ice-cold 80% methanol. After incubation at −80°C overnight, cell extracts were transferred to 2 mL tubes and centrifuged at 14,000 g for 20 min. Then, the supernatants were transferred and dried by vacuum. Then, a Dionex Ultimate 3000 UHPLC (Thermo Fisher Scientific, Waltham, MA) coupled with a Q Exactive was used to perform LC separation. In positive mode, an Atlantis HILIC silica column (2.1 × 100 mm, Waters) was used. Mobile phase A was prepared by dissolving 0.63 g of ammonium formate in 50 mL of HPLC-grade water and then adding 950 mL of HPLC-grade acetonitrile and 1 μL of formic acid. Mobile phase B was prepared by dissolving 0.63 g of ammonium formate in 500 mL of HPLC-grade water, followed by 500 mL of HPLC-grade acetonitrile and 1 μL formic acid. Separation was initiated at 1% mobile phase B with a flow rate of 300 μL/min. The gradient was as follows: 0 min, 1% B; 2 min, 1% B; 3.5 min, 20% B; 17 min, 80% B; 17.5 min, 99% B; 19 min, 99% B; 19.1 min, 1% B; 20 min, 1% B. In negative mode, a BEH Amide column was applied (2.1 × 100 mm, Waters). Mobile phase A was prepared by dissolving 0.39 g of ammonium bicarbonate in 1 L of HPLC-grade water (pH~8.0). Mobile phase B was HPLC-grade acetonitrile. The gradient started at 1% mobile phase B with a flow rate of 250 μL/min as follows: 0 min, 1% B; 3 min, 1% B; 10 min, 99% B; 17 min, 99% B; 17.1 min, 1% B; and 20 min, 1% B. Untargeted metabolite screening was performed on a Q Exactive Orbitrap mass spectrometer (Thermo Fisher Scientific, San Jose, CA) after calibration following the manufacturer's guidelines. The detailed mass spectrometer parameters are as follows: spray voltage, 3.5 kV for positive and 2.5 kV for negative; capillary temperature, 320°C; sheath gas flow rate (arb), 35; aux gas flow rate (arb), 10; mass range (*m/z*), 70–1050 for positive and 80–1200 for negative; full ms resolution, 70,000 for positive and 60,000 for

negative; MS/MS resolution, 17,500 for positive and 30,000 for negative; TopN, 10; NCE, 15/30/45; duty cycle, 1.2 s.

Transcriptomics

A total of 5× 10^6 cells in the logarithmic growth phase were prepared, and the medium was removed and cleaned quickly with PBS buffer. TRIzol reagent was added and exposed to all surfaces with growing cells and fully digested. The prepared samples were sent to Novogen Technologies for transcriptome sequencing analysis, and raw files and clean data were returned.

Retro-pull-down experiment

In brief, 20 μL Ni-NTA agarose beads were incubated with 1 mL His-SHMT2 (0.5 mg/mL) or its buffer control (20 mM HEPES, 200 mM NaCl, 5 mM DTT and 10% glycerol, pH 7.5) at 4°C for 2 h. The beads were washed with PBST (pH = 7.4, 0.5% Tween 20 with 20 mM imidazole) 3 times, and 800 μL of GA solution (20 μM in PBS, pH = 7.4) was added and incubated at 4°C for 16 h. Then, the supernatant was collected after centrifugation at 800 *g* for 2 min. Subsequently, 800 μL elution buffer (200 mM imidazole in PBS) was added, incubated for 10 min and collected after centrifugation at 800 *g* for 2 min. Concentrations of GA in supernatant or elution buffer were analyzed by LC/MS.

Recombinant human SHMT2 expression and purification

The cDNA encoding human mitochondrial SHMT2 (isoform 3; NCBI reference sequence NP_001159831.1, named SHMT2α, with an amino acid sequence identical to that of isoform 1, but lacking the N-terminal import signal) was cloned into a pETDuet-1 vector and transformed into *E. coli* strain BL21 (DE3). Cultures were grown at 37°C with shaking to an OD_{600} of 0.6–0.8, induced with 0.5 mM IPTG. Cells were grown overnight at 16°C, harvested by centrifugation, washed and resuspended in 30 mL of lysis buffer (20 mM Tris-HCl pH 8.0, 500 mM NaCl and 10 mM imidazole). Protein was first purified from crude lysate by Ni-affinity chromatography and then dialyzed in buffer (20 mM Tris,150 mM NaCl, 10% glycerol) followed by thrombin protease digestion (Invitrogen) overnight. The lysate was loaded onto a second Ni affinity column, eluted, and finally purified by size-exclusion chromatography (Superdex 200 column, GE Healthcare) and assessed for purity (>95%) by SDS/PAGE analysis with Coomassie staining. The proteins were concentrated to 20 mg/mL in a buffer with 20 mM HEPES, 200 mM NaCl, 5 mM DTT and 10% glycerol, pH 7.5, for crystallization.

Cellular thermal shift assay

Cells were grown to 80% confluency before being treated with 300μMGA (or DMSO control) for 5 h. Subsequently, they were harvested by trypsin and resuspended in PBS (pH = 7.4). Then the cells were aliquoted into PCR tubes and heated for 5 min to 46, 48, 50, 52, 54, 56, 58, 60, or 64°C. The cells were lysed by 3 cycles of freeze–thawing with liquid nitrogen and centrifugation at 17,000 g for 15 min. The soluble fractions were analyzed by SDS–PAGE and immunoblotted with anti-SHMT2 antibody.

SPR analysis

The SPR analyses were carried out using a BI-Acore ST200 system with the CM5 chips at 25°C. For the SPR measurements, the SHMT2 protein was prepared in PBST buffer consisting of 1.05× PBS (142.8 mM NaCl, 2.7 mM KCl, 8.4 mM Na_2HPO_4, 2.1 mM KH_2PO_4, pH 7.4) and 0.005% Tween 20. The SHMT2 protein was immobilized on the CM5 chip at ∼17,000 response units. The blank channel served as the negative control. Gradient concentrations of compounds were flowed over SHMT2 protein on the chip surface at 30 μL/min, and the amount of bound compounds in response units was recorded for comparison. For dissociation constant (KD) calculations, the data of compounds binding to SHMT2 were fitted to a Bivalent-Analyte binding model.

Fluorescence quenching assay

Fluorescence titrations were performed using a Lumina Fluorescence Spectrometer (hermo Fisher Scientific, MA) at 25°C with 5 nm excitation and emission bandwidths. The excitation wavelength was 274 nm, and the emission spectra were measured between 285 and 650 nm. Gradient concentrations of GA were titrated into 1 mM SHMT2 in HEPES buffer (20 mM HEPES, 200 mM NaCl, 5 mM DTT, pH 7.5).

Purine and pyrimidine derivatives analysis

HeLa cells were pretreated with increasing concentrations of GA for 12 h. The medium was then aspirated, and the cells were rinsed with 1 mL of PBS (pH 7.4) for 3 times. Adherent cells were detached from the flask with trypsin-EDTA, counted by countstar (Countstar BioTech, China), and pelleted by centrifugation (800 g, 5 min). Then metabolism was quenched by adding 2 mL of 80% methanol and sonicating in ice-cold water for 5 min. The supernatant was collected after centrifugation at 20,000 g for 20 min, drained by vacuum and stored at −80°C until analysis. Metabolite extracts were resuspended in 60 μL 60% acetonitrile (v/v), vortexed thoroughly and clarified by centrifugation (20,000 g, 20 min). Next, 50 μL of supernatant was transferred to an autosampler vial and analyzed by LC/MS.

LC/MS for GA, purine and pyrimidine quantification

The LC/MS method for GA and XMP quantification involved reversed-phase ion-pairing chromatography coupled by negative mode electrospray ionization to a stand-alone orbitrap mass spectrometer (AB SCIEX QTRAP 5500) with LC separation on an ACQUITY UPLC HSS T3 C18 (100 ×2.1 mm, 1.8 μm particle size) column using a gradient of solvent A (0.1% formic acid in water with 10 mM ammonium formate), and solvent B (100% acetonitrile). The gradient was 0 min, 0% B; 0.01 min, 40% B; 3.5 min, 60% B; 5 min, 80% B; and 8.0 min, 90% B. The injection volume was 2 μL, the flow rate was 400 μL/min, and the column temperature was 25°C. The scanning ion pairs were GA (469.2/425.2), AMP (346.5/211), CMP (322.5/279.5), GMP (362.5/211.3), and UMP (323.5/280.5). A standard curve of GA was generated with concentrations of 0.006, 0.012, 0.024, 0.049, 0.098, 0.195, 0.391, 0.781, 1.563, 3.125, 6.25, and 12.5 μg/mL of concentration by diluting GA in 50% ethanol. Based on the standard curve, the amount of GA in each sample was calculated and corrected for dilution.

Cellular apoptosis assays

PC-Annexin V with a 7-AAD Apoptosis Detection Kit was used for the direct detection of viable, early apoptotic, and late apoptotic cells by flow cytometry. SHMT2 KO or WT HeLa cells were seeded in 6-well plates at a density of 2×10^5 cells/well and treated with 150 mM GA for 12 h. The cells were collected and stained with APC-Annexin V and 7-AAD following the manufacturer's instructions for the apoptotic assays. The cell ratios in different areas were analyzed using BD FACS Calibur.

Crystallization, data collection and model building

Yellow needle-shaped native crystals were grown by the hanging-drop vapor diffusion method by mixing 1 μL of a 20 mg/mL solution of SHMT2 (20 mM HEPES, 200 mM NaCl, 5 mM DTT and 10% glycerol, pH 7.5) with 1 μL of reservoir solution containing 0.1 M sodium dihydrogen phosphate pH 6.5, 16% PEG 2000. Drops were equilibrated for 3 days at 20°C against 300 μL reservoir solution. The crystals of SHMT2-GZ were obtained by soaking native crystals in crystallization solution containing 0.1 M sodium dihydrogen phosphate pH 6.5, 16% PEG 2000, 5 mM of the relevant compound for 4 h and then transferred into a cryo-protectant solution comprising mother liquor and 20% (v/v) glycerol before flash-freezing in liquid nitrogen for data collection. Diffraction data were collected at 100 K in SSRF Beamline BL19U1 (Shanghai, China) with a wavelength of 1.000Å. Data were processed and scaled using the HKL2000 package. The X-ray diffraction of SHMT2-GZ crystals was 2.45Å. The structure was solved by molecular replacement using Phaser with SHMT2 structure (PDB ID code 6H3C) as an initial search model. Repeated cycles of manual building/rebuilding using Coot were alternated with rounds of refinement using Refmac5. The coordinates, parameter files, and molecular topology of GZ were generated by PRODRG. The coordinates and structure factors for SHMT2-GZ presented in this paper were deposited in the PDB under codes 7BYH.

Inhibition assay of SHMT2 using compounds

The assay was carried out at 25°C in reaction buffer (25 mM sodium sulfate, 50 μM pyridoxal 5′-phosphate hydrate (PLP), 50 mM HEPES buffer (pH 8.0)). GA was dissolved in DMSO, and the final concentration was varied (DMSO was 5%V/V) in the assay. In all assays, SHMT2 (5 μM) was mixed with GA/DMSO. After the addition of 50 mM DL-β-phenylserine, followed by rapid mixing the absorbance at 281 nm was measured by a Cytation™3 reader (BioTek, USA). All measurements were performed in triplicate and three independent experiments were performed.

Synthesis of GA derivatives

To a solution of GA (470 mg, 1 mmol) in dry dichloromethane (50 mL), ethanediamine (300 mg, 5 mmol) and 1-hydroxybenzotriazole (HOBT) (162 mg, 1.2 mmol) were added and stirred at 0°C for 30 min.

Subsequently, N-(3-Dimethylaminopropyl)-N′-Ethylcarbodiimide Hydrochloride (EDCI) (229.2 mg, 1.2 mmol) and N,N-Diisopropylethylamine (DIPEA) (387 mg, 3 mmol) were added, and stirred at 0°C for an additional 30 min. The solution was then stirred at room temperature overnight and monitored by TLC until complete. The reaction solution was washed with 0.5 M HCl aqueous solution 3 times and dried with anhydrous Na_2SO_4. After the removal of solvents under vacuum, the crude product was recovered and further purified by silica gel column chromatography (dichloromethane: methanol = 10:1) to give product GEN (320 mg, 62.50% yield) as a white powder. For the synthesis of GPN and GBN, diaminopropane (370 mg, 5 mmol) and butanediamine (440 mg, 5 mmol) were used, respectively, instead of ethanediamine. GPN (330 mg, 62.74% yield) was obtained as a white powder. GBN (315 mg, 58.33% yield) was obtained as a white powder.

Xenograft model

All mouse care and experimental procedures were conducted according to the Institutional Animal Care and Use Committee of Sichuan University (Approval number: 201820418). Nude Balb/c mice (male, 18–22 g, 6 weeks), which were provided by Beijing Huafukang Biosciences Co. Inc, were used to build the xenograft model. Stable cell lines with SHMT2 knockout (shSHMT2) or wild-type (shNC) were prepared. Three million cells in normal saline were subcutaneously injected into the flanks of each nude mouse on day 0. When tumors were palpable, the tumor-bearing mice were randomized into two groups: DMSO control and GA (30 mg/kg). The mice were intraperitoneally injected with GA (or DMSO control) every three days and tumor size and body weight were measured every 6 days during the experimental period. Tumor volumes were calculated using the following formula: volume ($millimeters^3$) = length × $width^2$.

QUANTIFICATION AND STATISTICAL ANALYSIS

MS data processing

Mass spectra were searched against the human UniProt database (20,239 entries, 2017/09) using the MaxQuant (version 1.5.3) computational platform(Cox and Mann, 2008). Trypsin was used as the proteolytic enzyme with two missed cleavage sites allowed. N-acetylation of protein and oxidation of methionine were set as variable modifications, and cysteine carbamidomethylation was set as the fixed modification. The mass error was set to 10 ppm for precursor peptide ions and 0.02 Da for fragment ions and peptides with a false discovery rate (FDR) lower than 1% were accepted.

Data analysis of the GA treated or SHMT2 knockout proteome

Intensities were extracted and normalized based on their total intensity to correct the sample loading difference, and zero intensity proteins, single-peptide proteins, reverse and contaminant were excluded. Proteins with good reproducibility (Student's *t*-test, $p > 0.1$) were chosen for further analysis. The upregulated proteins were filtered by an intensity ratio >1.25 (experiment/control) and p value <0.05 (Student's *t*-test). Likewise, proteins with a ratio <0.8 and p value <0.05 were regarded as downregulated. The differentially expressed proteins were analyzed for their related biological processes by the DAVID platform (V6.8) (Huang da et al., 2009). GSEA was conducted on the differentially expressed proteins using the tumor hallmark database (Version: h.all.v6.2.symbols.gmt [Hallmarks]) (Subramanian et al., 2005). Pearson correlation coefficient analysis was used to confirm the difference and similarity between SHMT2-knockout and GA-treated HeLa cells.

Data analysis of GA target proteins

For label-free quantification in target protein analysis, matching between runs was performed in MaxQuant software, and quantification was performed using the label-free quantification (LFQ) algorithm. Single-peptide proteins, zero intensity proteins in the GA probe group, quantified proteins in the blank control group, reverse and contaminant were all excluded. Those proteins with p-value <0.01 (GA-probe/competition, Student's *t*-test) and average intensity ratio >1.5 (GA-probe/competition) were chosen as binding proteins of GA, and for further protein– protein interaction (PPI) analysis by Metascape (Zhou et al., 2019).

Transcriptomics analysis

The human genome HG19 Reseq annotation was downloaded from the UCSC database website, and the sequence from the clean data was read and mapped into the human genome HG19. Quantitative transcripts were quantitated with FEATURES COUNTS quantitative software to obtain the COUNT raw data matrix. Count was calculated as TPM by R (3.6.1), and low abundance values with TPM mean values less

than 1 were screened out. The DESEQ2 package was used for log2 logarithmic conversion of TPM values and screening of differential genes.

Statistical analysis

Statistical analyses were performed using Microsoft Excel 2016, Graph Pad Prism version 9.0.0, or the R 3.6.1 statistical program as indicated in the figure legends. To compare two groups of independent samples two-tailed Student's *t*-test was used. For multiple comparisons between groups, one-way ANOVA or two-way ANOVA analysis with Bonferroni-corrected multiple comparisons were applied. Differences were considered statistically significant if $p < 0.05$. ns represents no significance, * represents $p < 0.05$, ** represents $p < 0.01$, *** represents $p < 0.001$, and **** represents $p < 0.0001$.